Core cross-linked polymeric micelles based on polypept(o)ides: from secondary structure formation of polypeptides to functional cross-linking strategies for polymeric micelles

Bauer, T.A.

5

Complex Structures Made Simple - Continuous Flow Production of Core Cross-Linked Polymeric Micelles for Paclitaxel Pro-Drug-Delivery

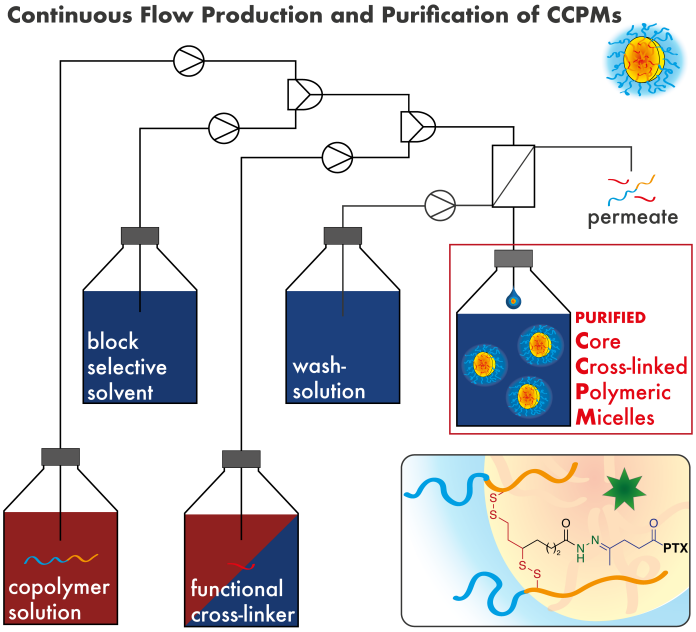

to be submitted to *Advanced Materials*.

Complex Structures Made Simple - Continuous Flow Production of Core Cross-Linked Polymeric Micelles for Paclitaxel Pro-Drug-Delivery

Tobias A. Bauer[a, b], Jonas Schramm[c], Federico Fenaroli[d], Svenja Siemer[e], Christine I. Seidl[a, b], Svenja Morsbach[f], Regina Bleul[c], Roland Stauber[e], Michael Maskos[c], Matthias Barz[a, b,*]

[a] Leiden Academic Centre for Drug Research (LACDR), Leiden University, Einsteinweg 55, 2333 CC Leiden, The Netherlands

[b] Department of Chemistry, Johannes Gutenberg University Mainz, Duesbergweg 10-14, 55128 Mainz, Germany

[c] Fraunhofer Institute for Microengineering and Microsystems, Carl-Zeiss-Str. 18-20, 55129, Mainz, Germany

[d] Department for Biosciences, University of Oslo, Blindernveien 31, 0371 Oslo, Norway

[e] Molecular and Cellular Oncology/Nanobiomedicine, ENT Department, University Medical Center Mainz, Langenbeckstraße 1, Mainz, Germany

[f] Max Planck Institute for Polymer Research, Ackermannweg 10, 55128 Mainz, Germany

to be submitted to *Advanced Materials*.

Abstract

Translating innovative nanomaterials to products requires efficient manufacturing techniques that ease large-scale and high-throughput synthesis with high reproducibility. Drug carriers in medicine embrace a complex subset of tasks calling for functionality yet robust concepts. Here, we report the synthesis of core cross-linked polymeric micelles (CCPMs) in a continuous flow process, which combines the commonly separated steps of micelle formation, core cross-linking, and purification into a single device. Redox-responsive CCPMs are formed from thiol-reactive polypept(o)ides of polysarcosine-*block*-poly(*S*-ethylsulfonyl-L-cysteine) and functional cross-linkers based on dihydrolipoic acid hydrazide for pH-dependent release of paclitaxel. The precisely controlled microfluidic self-assembly process allows the production of spherical micelles (D_h = 35 nm) while avoiding organic solvents and additives with unfavorable toxicity profiles. Self-assembly and functional cross-linking *via* slit interdigital micromixers produce 350-700 mg of CCPMs/h per single system, while purification by online tangential flow filtration successfully removes impurities (unimer ≤ 0.5%). The formed paclitaxel-loaded CCPMs (PTX@CCPMs) possess the desired pH-responsive drug release profile, display stable drug encapsulation, an improved toxicity profile compared to Abraxane, as well as therapeutic efficiency in the B16F1-xenotransplanted zebrafish larvae model. Therefore, the combination of reactive polymers, functional cross-linkers, and microfluidics enables the continuous-flow synthesis of therapeutically active CCPMs.

Keywords

polymeric micelles • polypept(o)ides • micromixer •continuous flow • cross-linking • stimuli-responsive

Introduction

Envisioning Paul Ehrlich's idea of the magic bullet, nanocarriers were designed to provide specificity, stability, and solubility to active pharmaceutical ingredients (APIs).[1–3] Due to their small size and high drug loading capacity, polymeric micelles have been thoroughly investigated for the delivery of small-molecule drugs such as anthracyclines and taxanes.[4–8] When non-specific interactions are absent and a long half-life in the bloodstream permits slow accumulation in diseased tissue, the selective biodistribution of the encapsulated API can be achieved enabling higher maximum tolerated doses and improved therapeutic efficiency.[3,9–11] To prevent premature drug release and carrier disintegration immediately after the administration into the bloodstream, additional stabilization strategies are required.[12–14] Core cross-linked polymeric micelles (CCPMs) have thus evolved as the second generation of polymeric micelles.[14] Moreover, (bio-) reversible drug conjugation strategies have been described that allow for external or disease-related drug release from CCPMs.[15–18] As the most promising example, CCPMs containing pH-cleavable docetaxel (CPC634) are currently under clinical evaluation for the treatment of platinum-resistant ovarian cancer in phase II (NCT03742713).[11,19,20]

The production of CCPMs typically involves the self-assembly of reactive block copolymers, cross-linking, and purification but requires facile, robust, and scalable manufacturing.[21] By combining the shielding properties of polysarcosine (pSar) with the inherent functionality and reactivity of polypeptides, the hybrid systems thereof, so-called polypept(o)ides, have attracted increasing attention.[22–24] Polypept(o)ides can be prepared by living amine-initiated ring-opening *N*-carboxyanhydride (NCA) polymerization leading to well-defined polymers with narrow dispersity.[25–27] Polysarcosine, poly(*N*-methyl glycine), is hydrophilic, non-charged, and exclusively a weak hydrogen bond acceptor that adopts a random coil structure in aqueous solutions, meeting the characteristics for protein resistant materials.[28–30] Besides similar solution properties compared to poly(ethylene glycol) (PEG), pSar showed an improved safety profile, characterized by a reduced induction of cytokine release and evasion from accelerated blood clearance phenomenon.[28,31–33] In combination with pSar as the shell material, poly(*S*-ethylsulfonyl-L-cysteine) (pCysSO_2Et) provides multi-functionality to CCPMs.[34,35] The thiol-reactive *S*-alkylsulfonyl group allows for NCA polymerization and can be addressed for chemoselective disulfide bond

formation, leading to CCPMs with tunable morphology and core functionality.[35–38]

While microfluidics have evolved to the state-of-the-art technique for the production of lipid nanoparticles (LNP) and colloidal nanoparticles, polymeric micelles and in particular CCPMs are synthesized in batch-mode using either film rehydration, solvent exchange, temperature-induced aggregation or precipitation techniques, which grant access to well-defined particles at optimized conditions.[39–41] Beyond such methods, micromixers enable continuous-flow processes and offer automated manufacturing increasing production rates and reproducibility, whereby the closed setup facilitates sterile particle preparation.[42,43] In the micrometer-sized compartments self-assembly can be tuned *via* solvents and concentrations, while diffusive mixing of the fluid streams governs the transfer of solvents or reagents, and can be adjusted for optimal particle size and PDI.[44–46] Mixing by simple T- or Y-junctions mainly leads to single and thick fluid lamellae resulting in high mixing times.[47] To reduce the mixing time and gain precise spatial and temporal control, interdigital micromixers have been developed. In the slit-interdigital micromixer (SIMM), multi-lamination and geometric flow focusing lead to thin fluid lamellae and high flow velocities.[47,48] The short mixing times in interdigital micromixers could thus be used to control self-assembly kinetically, giving access to non-equilibrium structures as reported for polymersomes from non-vesicle forming polymers by Thiermann *et al.*[42,45,49] Although micromixers are the preferred technique for LNPs in nucleic acid delivery,[41,42,50–55] a complete setup for the continuous flow production of CCPMs including online purification has not been reported to the best of our knowledge. The combination of self-assembly, core cross-linking and purification by this methodology is highly desirable feature to enable larger-scale production and provide access to CCPM libraries for screening of drugs and combination therapies by nanomedicine.[56]

We now propose the two-step synthesis and purification of CCPMs in a continuous flow process with online tangential flow filtration, whereby functional cross-linkers permit the decoupled and bio-reversible conjugation of a paclitaxel pro-drug yielding drug-loaded CCPMs (PTX@CCPMs) for tumor therapy. Nanoparticle performance is evaluated in cell culture and xenotransplanted tumor-bearing zebrafish larvae and compared to Abraxane. Xenotransplant tumor-bearing zebrafish larvae have evolved as a complementary *in vivo* model

to reduce animal test in rodents, enabling high throughput screening in combination with pharmacokinetic and pharmacodynamic studies.[57–60]

Results and Discussion

The concept for the synthesis of stimuli-responsive CCPMs via the continuous flow process is based on the cross-linking of thiol-reactive polypept(o)ides with functional cross-linkers. As illustrated in Figure 1A, block copolymers of polysarcosine-*block*-poly(*S*-ethylsulfonyl-L-cysteine) (pSar-*b*-pCys(SO_2Et)) were assembled to polymeric micelles by solvent switch methods. In a second step, the *S*-ethylsulfonyl-groups were addressed by chemoselective disulfide bond formation with thiols.[34,35] The designed cross-linker based on lipoic acid grants access to functional groups for bio-reversible drug conjugation *via* pH-responsive hydrazone bonds. While high reaction rates have been reported for the chemoselective disulfide bond formation,[61] the bottlenecks for a potential large-scale production of CCPMs were identified as the considerable amounts of solvent required by dialysis-based processes and the purification of the product CCPMs from residual polymer and cross-linker *via* the laborious and time-consuming spin filtration procedure. Moreover, to obtain spherical morphologies from batch processes, chaotropic additives such as thiourea are required to disrupt secondary structure formation of the thiol-reactive pCys(SO_2Et) block to direct self-assembly.[35]

In this study, we report on a continuous flow process for the production of therapeutically active CCPMs to address the identified shortcomings. As shown by the process chart in Figure 1C, self-assembly and core cross-linking were conducted in two consecutive micromixers connected to the online purification by tangential flow filtration. In the first step, the solution of the copolymer in the organic solvent is mixed with water as the block selective solvent. In the second micromixer, the cross-linker dissolved in ethanol/water mixtures is added to the micelle solution from micromixer #1. Since ethanol does not dissolve pCys(SO_2Et) the mixing step does not impair micelle integrity. For purification by tangential flow filtration regenerated cellulose membranes (molecular weight cut-off (MWCO), 30 kDa) and water were employed yielding CCPMs in the retentate. The permeate (or waste) contains residual polymer, cross-linker, organic solvents, and tris(2-carboxyethyl)phosphine oxide, which was used to generate dihydrolipoic acid hydrazide from the parent disulfide (3).

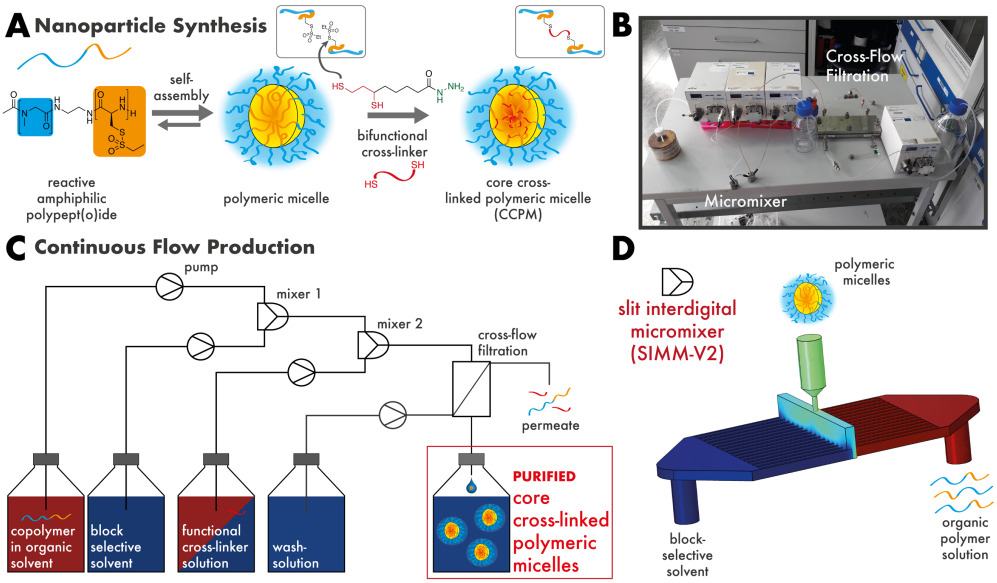

Figure 1. Synthesis of core cross-linked polymeric micelles in a continuous flow process. (**A**) Amphiphilic thiol-reactive pSar-*b*-pCys(SO_2Et) polypept(o)ides are assembled to polymeric micelles *via* solvent switch followed by cross-linking by chemoselective disulfide bond formation with dihydrolipoic acid hydrazide. (**B**) Photo of the continuous flow setup (**C**) Chart of the continuous flow process. Reagent mixing by slit interdigital micromixers operated by HPLC pumps, and online particle purification by tangential flow filtration (MWCO, 30 kDa; regenerated cellulose membrane). (**D**) Schematic illustration of the slit interdigital micromixer used for self-assembly and cross-linking (SIMM-V2).

The complete setup of the continuous flow process and the online tangential flow filtration is displayed in Figure 1B. The micromixer for self-assembly was directly connected to the reactor for the cross-linking step, and both were operated by HPLC pumps. After cross-linking, the particles entered the tangential flow filtration, where a four-fold dilution was performed, and the 10-fold concentrated particle solution could be collected (β_{CCPM} = 14 g·L^{-1}). All mixing processes were performed in a slit-interdigital micromixer V2 (SIMM; Fraunhofer IMM), which allows for asymmetric flow ratios (e.g., 1-9) and shows a low tendency for aggregate formation (Figure S2). The SIMM splits the two fluid streams into eight lamellae fusing in an interdigital fashion (Figure 1D). The optimal overall flow rate was 10-12 mL·min^{-1} at which the microstructures (inner volume 8 µL) direct laminar flow at the beginning and rather turbulent flow near the outlet capillary after geometric flow focusing (outlet diameter 60 µm; Reynolds number ~ 4500;

total mixing time 40 ms). To dissolve pSar-*b*-pCys(SO_2Et) dimethyl sulfoxide (DMSO) was selected over *N*,*N*-dimethylacetamide (DMAc) used previously since the higher polymer solubility supports the formation of well-defined micelles (Figure S3).[35,62,63] According to the guidelines of the International Council for Harmonization (ICH), DMSO and ethanol are classified as substances with a low toxic potential (class 3 solvent), allowing for a process without potentially hazardous solvents. In addition, potentially carcinogenic thiourea (TU) was rendered unnecessary for the synthesis of spherical particles from pSar-*b*-pCys(SO_2Et) using the continuous flow process.

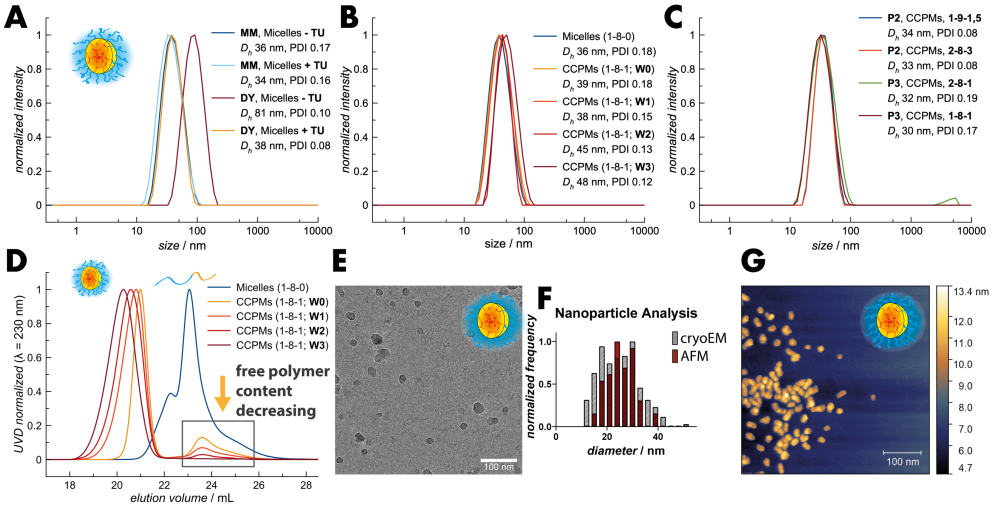

Figure 2. Analysis of micelles and CCPMs produced by continuous flow process. (**A**) DLS analysis of micelles and CCPMs by self-assembly or micromixer process. (**B**) DLS analysis of micelles and CCPMs before (W0) and after purification by tangential filtration cycles (W1-W3). (**C**) DLS analysis of CCPMs formed by varied relative flow rate ratios (**D**) HFIP-GPC analysis of micelles and CCPMs before and after purification by tangential-flow filtration cycles (W0 - W3). (**E**) Cryo-EM image of micromixer-CCPMs. (**F**) Diameter of micromixer-CCPMs determined by AFM and cryo-EM image analysis. (**G**) AFM image of micromixer-CCPMs.

As shown in Figure 2, the micromixer process (MM) yielded polymeric micelles with small diameters (D_h = 34-36 nm) and narrow PDIs ≤0.17, irrespective of chaotropic additives (+/- TU). Conversely, larger structures were obtained when the dialysis procedure (DY) was applied without TU, resulting in worm-like micelles referring to secondary structure-driven self-assembly of the pCys(SO_2Et)

block.[35,62] Within the micromixer, the fast and precisely controlled solvent exchange thus overruled the secondary structure formation as the guiding element.[46,64] Consequently, small spherical nanoparticles were obtained from pSar-*b*-pCys(SO_2Et) in the micromixer that were identical to the CCPMs from the dialysis procedure with TU, in which anti-parallel ß-sheets were disrupted by saturation of the hydrogen bonds *via* the chaotropic agent.[35] Cross-linking with dihydrolipoic acid hydrazide in SIMM #2 did not affect the particle size or PDI, as shown in Figure 2B (CCPM, W0). Moreover, the continuous flow process was robust to alterations in the polymer block lengths and in the relative flow rate ratios (Figure 2C, Figure S4). For each device 350-700 mg of CCPMs could be obtained per hour, whereby channel fouling was not observed. Since the microstructures are crucial for the performance of micromixers, scale-up can best be performed by parallelization, i.e., numbering up.[48] Purification of the CCPMs by tangential flow filtration slightly increased the particle diameter during the process (39 nm to 48 nm) yet slight decreasing the PDI to 0.1. The tangential flow filtration ultimately lead to CCPMs with free polymer contents below the limit of detection in HFIP-GPC analysis (≤ 0.5%) (Figure 2D, Figure S5), which further underlines the stability of the CCPMs. Beyond small molecule contamination, purification from unconjugated polymer is of significance for most biomedical applications of CCPMs as free amphiphilic unimers cause unspecific interaction with plasma proteins.[65] Analysis of the CCPMs by cryogenic transmission electron microscopy (cryo-EM) and atomic force microscopy (AFM) confirmed the spherical morphology of the purified nanoparticles. The diameters of 24.8 ± 7.6 nm (cryo-EM) and 25.7 ± 5.3 nm (AFM) were in good agreement with (multi-angle) DLS analysis, where no angle dependency was observed (Figure 2B, Figure 2E-G, and Figure S6-S9).

The presented continuous flow process successfully yielded CCPMs from pSar-*b*-pCys(SO_2Et) at varied chain lengths and flow rate ratios when the functional cross-linker dihydrolipoic acid hydrazide was used. In fact, the selection of the cross-linker was an important parameter for the process. If larger and more hydrophobic cross-linkers were used, aggregate formation and channel fouling were readily observed in the micromixer (Figure S10-S11). As a solution, functional cross-linkers allowed decoupling of carrier synthesis and drug conjugation. Each process could thus be optimized separately with the potential to achieve higher yields at reduced synthetic effort and cost. This relies on stable nanocarriers that do not aggregate during drug loading and purification, a task

well suitable for core cross-linked particles.[66] As illustrated in Figure 3, the functional cross-linker lipoic acid hydrazide was designed to conjugate ketone-modified PTX-LEV to CCPMs by hydrazone bond formation. Hydrazone bonds remain intact at physiological pH and enable stimuli-responsive drug release by cleavage at endo-lysosomal pH values.[17] In combination with the disulfide cross-links, PTX-loaded CCPMs (PTX@CCPMs) featured dual stimuli-responsive drug release accounting for optimal API delivery.[67] The contemporaneous availability of PTX and cysteine was not expected to interfere with the drug's mechanism of action but may be relevant for delivery of APIs such as cisplatin.[68,69]

Two techniques were evaluated for PTX conjugation to CCPMs: film-hydration and reaction in DMSO. For the latter, DMSO was employed to solubilize the drug and induce swelling of the micellar core. To provide an additional driving force for drug loading into the core, the film-hydration technique was adapted and modified from vesicle and micelle preparation methods. In both cases, excess PTX-LEV was removed by centrifugation and filtration, and the final drug-loaded nanoparticles were obtained in aqueous solution after reconstitution with sterile water from lyophilization. The conjugation of PTX-LEV to lipoic acid hydrazide-functionalized CCPMs was verified by NMR analysis, whereby characteristic signals of the hydrazone-bond formation could be detected (Figure S12). Further, both loading techniques lead to PTX@CCPMs with narrow PDIs below 0.1 (Figure 3A). In addition, the particle sizes were not significantly affected by the drug loading *via* film-hydration (PTX@CCPMs-F) or reaction in DMSO (PTX@CCPMs-D). Since vast swelling is inhibited by the high cross-linking density within the micellar core, the comparable sizes account for absence of aggregation.

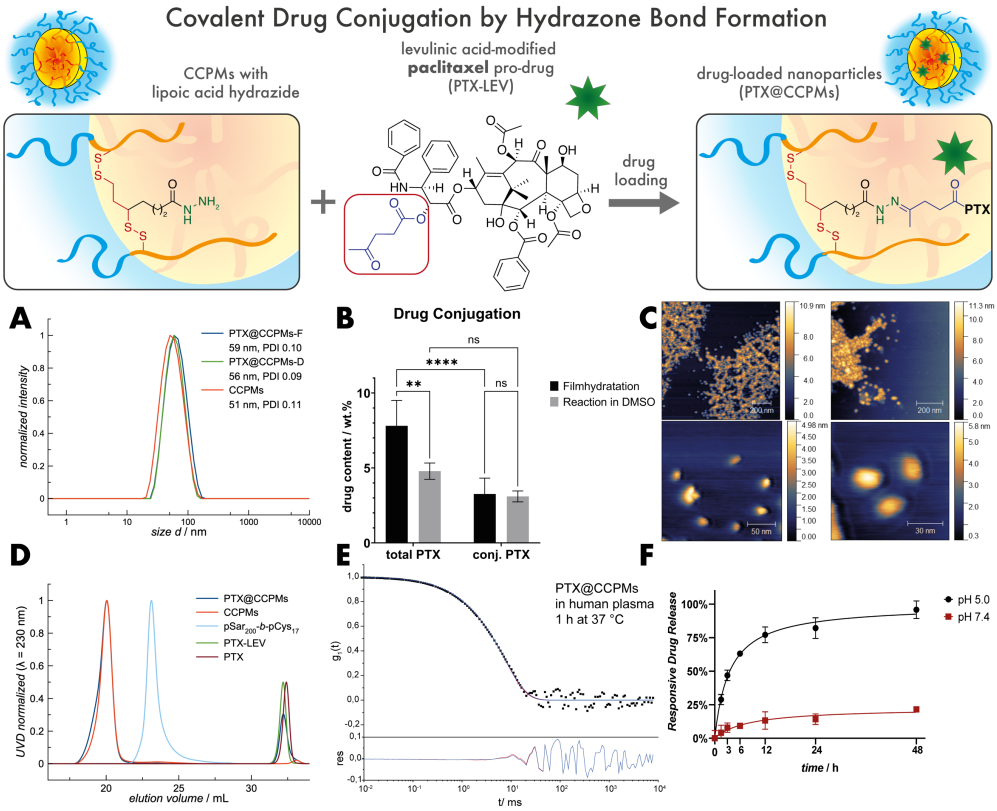

Figure 3. PTX pro-drug conjugation to functional CCPMs by hydrazone bond formation (PTX@CCPMs). (**A**) DLS analysis showed narrow PDIs for CCPMs before and after drug loading, purification, lyophilization and reconstitution in water. No significant differences were observed when film-hydration (PTX@CCPMs-F) or reaction in DMSO (PTX@CCPMs-D) were applied for drug conjugation. (**B**) Quantification of total and conjugated amount of PTX (in wt.%) by RP-HPLC. Data reported as N ± standard error of the mean for at least 4 independent experiments. Two-way ANOVA (*): *p < 0.05, **p < 0.01, ***p < 0.001, ****p < 0.0001. (**C**) AFM images of PTX@CCPMs confirmed spherical particle morphology. (**D**) HFIP-GPC analysis confirmed particle integrity after drug-loading. (**E**) Multi angle DLS of PTX@CCPMs in undiluted human plasma: autocorrelation function $g_1(t)$ given for a representative measurement angle of 30°. The fits with (blue line) and without (red line) aggregation term (upper graph), and the derived residuals for the fit w/o aggregate and correlation function (lower graph) indicated no significant aggregation. (**F**) Stimuli-responsive drug release at 37 °C in biologically relevant osmolar conditions (pH = 5.0 or 7.4), evaluated by RP-HPLC (N = 3).

As shown in Figure 3B, total paclitaxel contents of 7.81 ± 1.51 wt.% and 4.79 ± 0.47 wt.% were determined for PTX@CCPMs-F and PTX@CCPM-D by RP-HPLC, while similar amounts of approx. 3 wt.% were conjugated covalently. Film-hydration thus leads to significantly higher total drug loading ($p < 0.0001$) compared to the reaction in DMSO. The comparable amounts of conjugated drug point toward a densely packed micellar core hampering the reaction of the cross-linker with the relatively large drug molecule.[44,70] In fact, loading polymeric micelles with taxanes frequently leads to low drug contents below 3 wt.% unless specific drug-polymer interactions are employed.[71–73] When the conjugation reactions were performed in DMF or $CHCl_3$ which also solubilize the copolymer, no drug loading could be identified. In addition, reactions in DMSO in the presence of buffer containing aniline, which has been reported to catalyze the hydrazone bond formation for small molecules in solution, did not improve but decrease drug loading.[74,75] Since higher drug-loading was achieved by film-hydration, only these particles were further investigated. When analyzed by AFM, spherical structures with sizes well below 50 nm were revealed for PTX@CCPMs (Figure 3C). Drug loading by film-hydration did thus not affect the morphology of the nanoparticles. In addition, the GPC confirmed the integrity of the cross-linked nanomedicine, as no significant traces of homopolymer could be detected after incubation in HFIP for 1 h (Figure 3D). For passive targeting of diseased tissue *via* the enhanced permeability and retention (EPR) effect or related phenomena, stable circulation in the blood stream without premature carrier disintegration and drug release is a basic requirement, which stimulated the development of CCPMs.[76] Unspecific interaction of the carrier with components of the blood plasma shall thus be prevented.[77] Consequently, PTX@CCPMs were analyzed by multi-angle DLS in human blood plasma following the procedure established by Rausch *et al.*[78] Here, no significant aggregation could be detected after incubation at 37°C for 1 h (Figure 3E and Figure S13). To study the stimuli-responsive drug release, PTX@CCPMs were incubated at physiological or endo-lysosomal pH and analyzed by RP-HPLC. As shown in Figure 3F, PTX-LEV was quickly released from the nanoparticle providing 46.9 ± 3.2% after 3 h, and up to 95.8 ± 5.4% cumulative drug release after incubation at pH 5 for 48 h. Vice versa, a slower release profile was observed in PBS (pH 7.4), whereby only 7.9 ± 2.8% and 21.5 ± 1.1% could be detected after incubation for 3h and 48 h. This underlines the stimuli-responsive release mediated by the pH-sensitive hydrazone bone.[17,79,80]

For biologic evaluation PTX@CCPMs were tested in cell culture and in zebrafish embryos, and the performance was compared to Abraxane as internal therapeutic reference (Figure 4). Abraxane is considered as the first FDA-approved nanomedicine, whereby PTX is formulated with human serum albumin replacing castor oil and ethanol used in Taxol.[81,82] As shown in Figure 4A, the time-dependent toxicity varied among the three formulations (Figure 4B and Figure S15B). At equal drug concentration, free PTX in DMSO induced severe toxicity immediately. In contrast, Abraxane and PTX@CCPMs showed reduced or modest toxicity at the early 2 h time point. After 48 h, no differences could be observed for the cell viability among all groups. In addition, PTX@CCPMs and Abraxane showed similar IC_{50} values of 20.6 and 14.9 nm in HeLa cells (Figure 4A), both comparable with the free drug dissolved in DMSO (11.9 nm) (Figure S14). Referring to the release profile of PTX@CCPMs (Figure 3F), the slower kinetics matched the expectation, as the nanomedicine requires cleavage of the pro-drug before inducing toxicity.[14] The identical cellular toxicity after 48 h, thus underlined the successful PTX release.

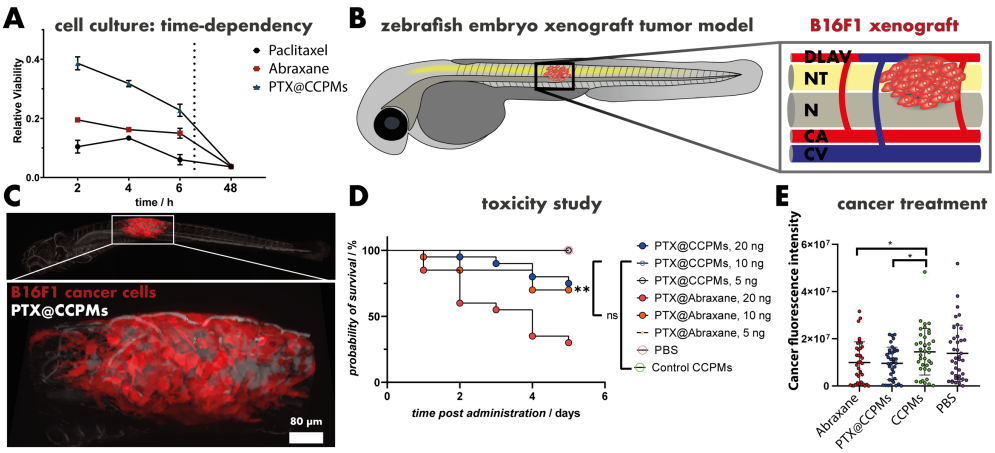

Figure 4. Biologic evaluation of PTX@CCPMs. (**A**) Time-dependent toxicity of paclitaxel formulations in HeLa cells. (**B**) Schematic illustration of the B16F1 mouse melanoma cell xenograft tumor model in zebrafish embryos. Cancer cells were injected in the trunk central region indicated by the black rectangle. The magnification shows neural tube (NT), noto-chord (N), dorsal longitudinal anastomotic vessel (DLAV), caudal artery (CA), and caudal vein (CV) with tumor formation after xenotransplantation in the neural tube.[83] (**C**) Fluorescence microscopy image of the PTX@CCPM (white) accumulation in the tumor-region of RFP expressing B16F1 mouse melanoma cell (red) xenotransplanted zebrafish embryos, 8 h post nanoparticle injection. (**D**) Toxicity study for paclitaxel formulations in

zebrafish embryos (without tumor). (**E**) Cancer treatment study for paclitaxel formulations in B16F1 bearing zebrafish embryos. The schematic illustration in (B) was adapted and modified from Kocere *et al.*[83]

For the consequent *in vivo* study, we chose the zebrafish larvae model. Zebrafish larvae are an emerging preclinical model allowing for rapid drug screening for novel therapeutic approaches against bacterial infections and cancer, substantially contributing to reducing animal testing in rodents.[58–60,83] In zebrafish larvae xenotransplanted with red fluorescent protein (RFP) expressing B16F1 mouse melanoma cells, PTX@CCPMs significantly accumulate in the tumor region within 8 h post injection according to fluorescence-based image analysis (Figure 4D and Figure S16).[57,84] At this time point, more than 40% of the injected dose were still in circulation and could be detected in the vasculature (Figure S17, Figure 4D, upper image, PTX@CCPM in white). The drug loading did not impair the circulation behavior of the carrier but slightly reduced nanoparticle clearance from the blood stream (Figure S17). The maximum tolerated dose of PTX@CCPMs and Abraxane was tested using healthy zebrafish embryos (Figure 4E). For PTX@CCPMs, up to 10 ng of PTX per fish could be administered without detectable toxicity at day 5 post injection. In comparison, application of PTX *via* Abraxane was less tolerated allowing for only 5 ng of PTX without inducing toxicity. The same trend for the survival rate was found for doses of 20 ng PTX administered by PTX@CCPMs and 10 ng of PTX *via* Abraxane. The more stable encapsulation of PTX in PTX@CCPMs thus reduced off-target toxicity of the API. These findings are in line with earlier reports on the reduced toxicity of doxorubicine encapsulated in polymersomes compared to the free drug tested in zebrafish embryos.[57] Ultimately, the nanomedicines were investigated in B16F1 tumor-bearing zebrafish embryos. Cancer cells were injected 24 h before the treatment, and the therapeutic efficacy was evaluated by fluorescence-based image analysis after 6 days. Tumor therapy was performed at equal toxicity using 10 and 5 ng PTX per fish administered by PTX@CCPMs or Abraxane compared to empty CCPMs or PBS. As shown in Figure 4F, both PTX treatments showed a reduction in cancer growth, whereby no statistical significances could be evaluated among PTX@CCPMs or Abraxane. In this preclinical study, Abraxane and PTX@CCPMs showed comparable performance, whereby the improved toxicity profile of PTX@CCPMs is a first indication for a beneficial patient compliance.

Taken together, the presented design concept for decoupling CCPM synthesis and drug loading enables continuous flow production of nanoparticles and stimuli-responsive encapsulation and conjugation of small molecule (pro-) drugs. Future research will be directed to explore this platform beyond the model drug PTX and for encapsulation of synergistic APIs realizing combination therapy.

Conclusion

We have established a continuous flow process for the synthesis of core cross-linked polymeric micelles aiming for precise control over the molecular properties of the next generation of nanomedicines. The core-shell architectures were produced by self-assembly and cross-linking in two consecutive slit interdigital micromixers using chemoselective disulfide bond formation of thiol-reactive polypept(o)ides (pSar-*b*-pCys(SO_2Et)) with functional cross-linkers. Online purification by tangential flow filtration was used for particle purification and could successfully reduce the amount of unconjugated polymer to below the limit of detection ($\leq$ 0.5%). Without any numbering up by parallelization, the process leads to 350-700 mg CCPMs/h. Due to the well-defined self-assembly kinetics, spherical micelles (D_h = 35 nm, PDI = 0.17) were obtained. Consequently, the continuous flow process could be performed in solvents with a low toxicity profile (DMSO, ethanol). After CCPM synthesis and purification, paclitaxel-levulinic acid was conjugated to the CCPMs *via* hydrazone bond formation with the lipoic acid cross-linker (PTX@CCPMs). The drug-loading did not affect the nanoparticle size and morphology while featuring pH-responsive drug release. In cell culture (HeLa, B16F1) and the zebrafish embryo xenograft model (B16F1), PTX@CCPMs showed similar performance compared to Abraxane, while the stable encapsulation in PTX@CCPMs reduced the toxicity of the paclitaxel *in vivo*. Committing to the strategy of decoupled CCPM synthesis and drug conjugation, future research will focus on tuning the release kinetics of APIs to establish combination therapies. The presented continuous flow process for the production and purification will ease the translation of CCPMs by enabling the straightforward synthesis of particle libraries under precisely controlled conditions.

Author Contribution

Conceptual design, polymer synthesis, cross-linker synthesis, drug conjugation, single-angle DLS measurements, AFM measurements, GPC measurements, and HPLC studies were performed by T.A.B. J.S. designed the continuous flow setup and executed CCPM synthesis and purification therein. F.F. performed *in vivo* experiments, S.S. and R.S. provided the in vitro experiments. C.I.S. and S.M. contributed multi-angle DLS measurements. R.B. and M.M. supervised the microfluidic experiments. The manuscript was written by T.A.B. and M.B. The project was supervised M.B.

Notes

The authors declare the following competing financial interest(s): Matthias Barz holds the patent Thiol-protected amino acid derivatives and uses thereof WO2015169908A1.

Acknowledgement

We acknowledge Christine Rosenauer for multi-angle DLS measurements, Holger Adam for AFM support and Dr. Rüdiger Berger for measurement of AFM images. We thank the Netherlands Centre for Electron Nanoscopy for the access and Dr. Willem Noteborn for cryo-EM measurements. T.A.B. would like to thank the HaVo Stiftung and the Max-Planck-Graduate-Center for financial support. T.A.B., C.I.S., M.M., and M.B. acknowledge the Deutsche Forschungsgemeinschaft (SFB1066) for funding.

References

(1) Bertrand, N.; Leroux, J. C. The Journey of a Drug-Carrier in the Body: An Anatomo-Physiological Perspective. *J. Control. Release* **2012**, *161* (2), 152–163.

(2) Lammers, T. SMART Drug Delivery Systems: Back to the Future vs. Clinical Reality. *Int. J. Pharm.* **2013**, *454* (1), 527–529.

(3) Lammers, T.; Kiessling, F.; Hennink, W. E.; Storm, G. Drug Targeting to Tumors: Principles, Pitfalls and (Pre-) Clinical Progress. *J. Control. Release* **2012**, *161* (2), 175–187.

(4) Cabral, H.; Miyata, K.; Osada, K.; Kataoka, K. Block Copolymer Micelles in Nanomedicine Applications. *Chem. Rev.* **2018**, *118* (14), 6844–6892.

(5) Murakami, M.; Cabral, H.; Matsumoto, Y.; Wu, S.; Kano, M. R.; Yamori, T.; Nishiyama, N.; Kataoka, K. Improving Drug Potency and Efficacy by Nanocarrier-Mediated Subcellular Targeting. *Sci. Transl. Med.* **2011**, *3* (64).

(6) Talelli, M.; Iman, M.; Varkouhi, A. K.; Rijcken, C. J. F.; Schiffelers, R. M.; Etrych,

T.; Ulbrich, K.; van Nostrum, C. F.; Lammers, T.; Storm, G.; Hennink, W. E. Core-Crosslinked Polymeric Micelles with Controlled Release of Covalently Entrapped Doxorubicin. *Biomaterials* **2010**, *31* (30), 7797–7804.

(7) Von Hoff, D. D.; Mita, M. M.; Ramanathan, R. K.; Weiss, G. J.; Mita, A. C.; Lorusso, P. M.; Burris, H. A.; Hart, L. L.; Low, S. C.; Parsons, D. M.; Zale, S. E.; Summa, J. M.; Youssoufian, H.; Sachdev, J. C. Phase I Study of PSMA-Targeted Docetaxel-Containing Nanoparticle BIND-014 in Patients with Advanced Solid Tumors. *Clin. Cancer Res.* **2016**, *22* (13), 3157–3163.

(8) Mukai, H.; Kato, K.; Esaki, T.; Ohsumi, S.; Hozomi, Y.; Matsubara, N.; Hamaguchi, T.; Matsumura, Y.; Goda, R.; Hirai, T.; Nambu, Y. Phase I Study of NK105, a Nanomicellar Paclitaxel Formulation, Administered on a Weekly Schedule in Patients with Solid Tumors. *Invest. New Drugs* **2016**, *34* (6), 750–759.

(9) Matsumura, Y.; Maeda, H. A New Concept for Macromolecular Therapeutics in Cancer Chemotherapy: Mechanism of Tumoritropic Accumulation of Proteins and the Antitumor Agent Smancs. *Cancer Res.* **1986**, *46* (8), 6387–6392.

(10) Maeda, H. Macromolecular Therapeutics in Cancer Treatment: The EPR Effect and Beyond. *J. Control. Release* **2012**, *164* (2), 138–144.

(11) Atrafi, F.; van Eerden, R. A. G.; van Hylckama Vlieg, M. A. M.; Oomen-de Hoop, E.; de Bruijn, P.; Lolkema, M. P.; Moelker, A.; Rijcken, C. J.; Hanssen, R.; Sparreboom, A.; Eskens, F. A. L. M.; Mathijssen, R. H. J.; Koolen, S. L. W. Intratumoral Comparison of Nanoparticle Entrapped Docetaxel (CPC634) with Conventional Docetaxel in Patients with Solid Tumors. *Clin. Cancer Res.* **2020**, *26* (14), 3537–3545.

(12) Lu, J.; Owen, S. C.; Shoichet, M. S. Stability of Self-Assembled Polymeric Micelles in Serum. *Macromolecules* **2011**, *44* (15), 6002–6008.

(13) Richtering, W.; Alberg, I.; Zentel, R. Nanoparticles in the Biological Context: Surface Morphology and Protein Corona Formation. *Small* **2020**, *16* (39), 1–8.

(14) Talelli, M.; Barz, M.; Rijcken, C. J. F. F.; Kiessling, F.; Hennink, W. E.; Lammers, T. Core-Crosslinked Polymeric Micelles: Principles, Preparation, Biomedical Applications and Clinical Translation. *Nano Today* **2015**, *10* (1), 93–117.

(15) Su, Z.; Liang, Y.; Yao, Y.; Wang, T.; Zhang, N. Polymeric Complex Micelles Based on the Double-Hydrazone Linkage and Dual Drug-Loading Strategy for PH-Sensitive Docetaxel Delivery. *J. Mater. Chem. B* **2016**, *4* (6), 1122–1133.

(16) Rijcken, C. J.; Snel, C. J.; Schiffelers, R. M.; van Nostrum, C. F.; Hennink, W. E. Hydrolysable Core-Crosslinked Thermosensitive Polymeric Micelles: Synthesis, Characterisation and in Vivo Studies. *Biomaterials* **2007**, *28* (36), 5581–5593.

(17) Sonawane, S. J.; Kalhapure, R. S.; Govender, T. Hydrazone Linkages in PH Responsive Drug Delivery Systems. *Eur. J. Pharm. Sci.* **2017**, *99*, 45–65.

(18) Bauer, T. A.; Eckrich, J.; Wiesmann, N.; Kuczelinis, F.; Sun, W.; Zeng, X.; Weber, B.; Wu, S.; Bings, N. H.; Strieth, S.; Barz, M. Photocleavable Core Cross-Linked Polymeric Micelles of Polypept(o)Ides and Ruthenium(II) Complexes. *J. Mater. Chem. B* **2021**, *9* (39), 8211–8223.

(19) Hu, Q.; Rijcken, C. J.; Bansal, R.; Hennink, W. E.; Storm, G.; Prakash, J. Complete Regression of Breast Tumour with a Single Dose of Docetaxel-Entrapped Core-Cross-Linked Polymeric Micelles. *Biomaterials* **2015**, *53*, 370–378.

(20) Biancacci, I.; Sun, Q.; Möckel, D.; Gremse, F.; Rosenhain, S.; Kiessling, F.; Bartneck, M.; Hu, Q.; Thewissen, M.; Storm, G.; Hennink, W. E.; Shi, Y.; Rijcken, C. J. F.; Lammers, T.; Sofias, A. M. Optical Imaging of the Whole-Body to Cellular Biodistribution of Clinical-Stage PEG-b-PHPMA-Based Core-Crosslinked Polymeric Micelles. *J. Control. Release* **2020**, *328*, 805–816.

(21) Barz, M. Complexity and Simplification in the Development of Nanomedicines. *Nanomedicine* **2015**, *10* (20), 3093–3097.

(22) Birke, A.; Huesmann, D.; Kelsch, A.; Weilbächer, M.; Xie, J.; Bros, M.; Bopp, T.; Becker, C.; Landfester, K.; Barz, M. Polypeptoid- Block -Polypeptide Copolymers: Synthesis, Characterization, and Application of Amphiphilic Block Copolypept(o)Ides in Drug Formulations and Miniemulsion Techniques. *Biomacromolecules* **2014**, *15* (2), 548–557.

(23) Birke, A.; Ling, J.; Barz, M. Polysarcosine-Containing Copolymers: Synthesis, Characterization, Self-Assembly, and Applications. *Prog. Polym. Sci.* **2018**, *81*, 163–208.

(24) Klinker, K.; Barz, M. Polypept(o)Ides: Hybrid Systems Based on Polypeptides and Polypeptoids. *Macromol. Rapid Commun.* **2015**, *36* (22), 1943–1957.

(25) Aliferis, T.; Iatrou, H.; Hadjichristidis, N. Living Polypeptides. *Biomacromolecules* **2004**, *5* (5), 1653–1656.

(26) Vayaboury, W.; Giani, O.; Cottet, H.; Deratani, A.; Schué, F. Living Polymerization of α-Amino Acid N-Carboxyanhydrides (NCA) upon Decreasing the Reaction Temperature. *Macromol. Rapid Commun.* **2004**, *25* (13), 1221–1224.

(27) Fetsch, C.; Grossmann, A.; Holz, L.; Nawroth, J. F.; Luxenhofer, R. Polypeptoids from N -Substituted Glycine N -Carboxyanhydrides: Hydrophilic, Hydrophobic, and Amphiphilic Polymers with Poisson Distribution. *Macromolecules* **2011**, *44* (17), 6746–6758.

(28) Weber, B.; Birke, A.; Fischer, K.; Schmidt, M.; Barz, M. Solution Properties of Polysarcosine: From Absolute and Relative Molar Mass Determinations to Complement Activation. *Macromolecules* **2018**, *51* (7), 2653–2661.

(29) Ostuni, E.; Chapman, R. G.; Holmlin, R. E.; Takayama, S.; Whitesides, G. M. A Survey of Structure-Property Relationships of Surfaces That Resist the Adsorption of Protein. *Langmuir* **2001**, *17* (18), 5605–5620.

(30) Lau, K. H. A.; Ren, C.; Sileika, T. S.; Park, S. H.; Szleifer, I.; Messersmith, P. B. Surface-Grafted Polysarcosine as a Peptoid Antifouling Polymer Brush. *Langmuir* **2012**, *28* (46), 16099–16107.

(31) Weber, B.; Seidl, C.; Schwiertz, D.; Scherer, M.; Bleher, S.; Süss, R.; Barz, M. Polysarcosine-Based Lipids: From Lipopolypeptoid Micelles to Stealth-like Lipids in Langmuir Blodgett Monolayers. *Polymers (Basel).* **2016**, *8* (12).

(32) Nogueira, S. S.; Schlegel, A.; Maxeiner, K.; Weber, B.; Barz, M.; Schroer, M. A.; Blanchet, C. E.; Svergun, D. I.; Ramishetti, S.; Peer, D.; Langguth, P.; Sahin, U.; Haas, H. Polysarcosine-Functionalized Lipid Nanoparticles for Therapeutic MRNA Delivery. *ACS Appl. Nano Mater.* **2020**, *3* (11), 10634–10645.

(33) Son, K.; Ueda, M.; Taguchi, K.; Maruyama, T.; Takeoka, S.; Ito, Y. Evasion of the Accelerated Blood Clearance Phenomenon by Polysarcosine Coating of Liposomes. *J. Control. Release* **2020**, *322* (March), 209–216.

(34) Schäfer, O.; Klinker, K.; Braun, L.; Huesmann, D.; Schultze, J.; Koynov, K.; Barz, M. Combining Orthogonal Reactive Groups in Block Copolymers for Functional Nanoparticle Synthesis in a Single Step. *ACS Macro Lett.* **2017**, *6* (10), 1140–1145.

(35) Klinker, K.; Schäfer, O.; Huesmann, D.; Bauer, T.; Capelôa, L.; Braun, L.; Stergiou, N.; Schinnerer, M.; Dirisala, A.; Miyata, K.; Osada, K.; Cabral, H.; Kataoka, K.; Barz, M. Secondary-Structure-Driven Self-Assembly of Reactive Polypept(o)Ides: Controlling Size, Shape, and Function of Core Cross-Linked Nanostructures. *Angew. Chemie Int. Ed.* **2017**, *56* (32), 9608–9613.

(36) Schäfer, O.; Huesmann, D.; Barz, M. Poly(S -Ethylsulfonyl- l -Cysteines) for Chemoselective Disulfide Formation. *Macromolecules* **2016**, *49* (21), 8146–8153.

(37) Muhl, C.; Schäfer, O.; Bauer, T.; Räder, H.-J.; Barz, M. Poly(S -Ethylsulfonyl- l -Homocysteine): An α-Helical Polypeptide for Chemoselective Disulfide Formation. *Macromolecules* **2018**, *51* (20), 8188–8196.

(38) Schäfer, O.; Klinker, K.; Barz, M.; Braun, L.; Huesmann, D.; Schultze, J. Combining Orthogonal Reactive Groups in Blockcopolymers for Functional Nanoparticle Synthesis in a Single Step. *ACS Macro Lett.* **2017**, *6*, 1140-1145.

(39) Marre, S.; Jensen, K. F. Synthesis of Micro and Nanostructures in Microfluidic Systems. *Chem. Soc. Rev.* **2010**, *39* (3), 1183–1202.

(40) Mai, Y.; Eisenberg, A. Self-Assembly of Block Copolymers. *Chem. Soc. Rev.* **2012**, *41* (18), 5969–5985.

(41) Zhang, H.; Zhu, Y.; Shen, Y. Microfluidics for Cancer Nanomedicine: From Fabrication to Evaluation. *Small* **2018**, *14* (28), 1–25.

(42) Johnson, B. K.; Prud'homme, R. K. Mechanism for Rapid Self-Assembly of Block Copolymer Nanoparticles. *Phys. Rev. Lett.* **2003**, *91* (11), 1–4.

(43) Dou, Y.; Wang, B.; Jin, M.; Yu, Y.; Zhou, G.; Shui, L. A Review on Self-Assembly in Microfluidic Devices. *J. Micromechanics Microengineering* **2017**, *27* (11).

(44) Tyrrell, Z. L.; Shen, Y.; Radosz, M. Fabrication of Micellar Nanoparticles for Drug Delivery through the Self-Assembly of Block Copolymers. *Prog. Polym. Sci.* **2010**, *35* (9), 1128–1143.

(45) Bleul, R.; Thiermann, R.; Maskos, M. Techniques to Control Polymersome Size. *Macromolecules* **2015**, *48* (20), 7396–7409.

(46) Keßler, S.; Drese, K.; Schmid, F. Simulating Copolymeric Nanoparticle Assembly in the Co-Solvent Method: How Mixing Rates Control Final Particle Sizes and Morphologies. *Polymer (Guildf).* **2017**, *126*, 9–18.

(47) Ziegenbalg, D.; Kompter, C.; Schönfeld, F.; Kralisch, D. Evaluation of Different Micromixers by CFD Simulations for the Anionic Polymerisation of Styrene. *Green Process. Synth.* **2012**, *1* (2), 211–224.

(48) Tonhauser, C.; Natalello, A.; Löwe, H.; Frey, H. Microflow Technology in Polymer Synthesis. *Macromolecules* **2012**, *45* (24), 9551–9570.

(49) Thiermann, R.; Bleul, R.; Maskos, M. Kinetic Control of Block Copolymer Self-Assembly in a Micromixing Device – Mechanistical Insight into Vesicle Formation Process. *Macromol. Chem. Phys.* **2017**, *218* (2), 1–9.

(50) Schoenmaker, L.; Witzigmann, D.; Kulkarni, J. A.; Verbeke, R.; Kersten, G.; Jiskoot, W.; Crommelin, D. J. A. MRNA-Lipid Nanoparticle COVID-19 Vaccines: Structure and Stability. *Int. J. Pharm.* **2021**, *601* (April), 120586.

(51) Chen, D.; Love, K. T.; Chen, Y.; Eltoukhy, A. A.; Kastrup, C.; Sahay, G.; Jeon, A.; Dong, Y.; Whitehead, K. A.; Anderson, D. G. Rapid Discovery of Potent SiRNA-Containing Lipid Nanoparticles Enabled by Controlled Microfluidic Formulation. *J. Am. Chem. Soc.* **2012**, *134* (16), 6948–6951.

(52) Rhee, M.; Valencia, P. M.; Rodriguez, M. I.; Langer, R.; Farokhzad, O. C.; Karnik, R. Synthesis of Size-Tunable Polymeric Nanoparticles Enabled by 3D Hydrodynamic Flow Focusing in Single-Layer Microchannels. *Adv. Mater.* **2011**, *23* (12), 79–83.

(53) Capretto, L.; Carugo, D.; Cheng, W.; Hill, M.; Zhang, X. Continuous-Flow Production of Polymeric Micelles in Microreactors: Experimental and Computational Analysis. *J. Colloid Interface Sci.* **2011**, *357* (1), 243–251.

(54) Belliveau, N. M.; Huft, J.; Lin, P. J.; Chen, S.; Leung, A. K.; Leaver, T. J.; Wild, A. W.; Lee, J. B.; Taylor, R. J.; Tam, Y. K.; Hansen, C. L.; Cullis, P. R. Microfluidic Synthesis of Highly Potent Limit-Size Lipid Nanoparticles for in Vivo Delivery of SiRNA. *Mol. Ther. - Nucleic Acids* **2012**, *1* (8), e37.

(55) von Bomhard, S.; Schramm, J.; Bleul, R.; Thiermann, R.; Höbel, P.; Krtschil, U.; Löb, P.; Maskos, M. Modular Manufacturing Platform for Continuous Synthesis and Analysis of Versatile Nanomaterials. *Chem. Eng. Technol.* **2019**, *42* (10), 2085–2094.

(56) Greco, F.; Vicent, M. J. Combination Therapy: Opportunities and Challenges for Polymer–Drug Conjugates as Anticancer Nanomedicines. *Adv. Drug Deliv. Rev.* **2009**, *61* (13), 1203–1213.

(57) Kocere, A.; Resseguier, J.; Wohlmann, J.; Skjeldal, F. M.; Khan, S.; Speth, M.; Dal, N. J. K.; Ng, M. Y. W.; Alonso-Rodriguez, N.; Scarpa, E.; Rizzello, L.; Battaglia, G.; Griffiths, G.; Fenaroli, F. Real-Time Imaging of Polymersome Nanoparticles in Zebrafish Embryos Engrafted with Melanoma Cancer Cells: Localization, Toxicity and Treatment Analysis. *EBioMedicine* **2020**, *58*, 102902.

(58) Dal, N.-J. K.; Kocere, A.; Wohlmann, J.; Van Herck, S.; Bauer, T. A.; Resseguier, J.; Bagherifam, S.; Hyldmo, H.; Barz, M.; De Geest, B. G.; Fenaroli, F. Zebrafish Embryos Allow Prediction of Nanoparticle Circulation Times in Mice and Facilitate Quantification of Nanoparticle–Cell Interactions. *Small* **2020**, *16* (5). 1906719.

(59) Fenaroli, F.; Repnik, U.; Xu, Y.; Johann, K.; Van Herck, S.; Dey, P.; Skjeldal, F. M.; Frei, D. M.; Bagherifam, S.; Kocere, A.; Haag, R.; De Geest, B. G.; Barz, M.; Russell, D. G.; Griffiths, G. Enhanced Permeability and Retention-like Extravasation of Nanoparticles from the Vasculature into Tuberculosis Granulomas in Zebrafish and Mouse Models. *ACS Nano* **2018**, *12* (8), 8646–8661.

(60) Sieber, S.; Grossen, P.; Detampel, P.; Siegfried, S.; Witzigmann, D.; Huwyler, J. Zebrafish as an Early Stage Screening Tool to Study the Systemic Circulation of Nanoparticulate Drug Delivery Systems in Vivo. *J. Control. Release* **2017**, *264* (August), 180–191.

(61) Schäfer, O.; Huesmann, D.; Muhl, C.; Barz, M. Rethinking Cysteine Protective Groups: S -Alkylsulfonyl- l -Cysteines for Chemoselective Disulfide Formation. *Chem. - A Eur. J.* **2016**, *22* (50), 18085–18091.

(62) Bauer, T. A.; Imschweiler, J.; Muhl, C.; Weber, B.; Barz, M. Secondary Structure-Driven Self-Assembly of Thiol-Reactive Polypept(o)Ides. *Biomacromolecules* **2021**, *22* (5), 2171–2180.

(63) Clay, N. E.; Whittenberg, J. J.; Leong, J.; Kumar, V.; Chen, J.; Choi, I.; Liamas, E.;

Schieferstein, J. M.; Jeong, J. H.; Kim, D. H.; Zhang, Z. J.; Kenis, P. J. A.; Kim, I. W.; Kong, H. Chemical and Mechanical Modulation of Polymeric Micelle Assembly. *Nanoscale* **2017**, *9* (16), 5194–5204.

(64) Thiermann, R.; Bleul, R.; Maskos, M. Kinetic Control of Block Copolymer Self-Assembly in a Micromixing Device – Mechanistical Insight into Vesicle Formation Process. *Macromol. Chem. Phys.* **2017**, *218* (2), 1–9.

(65) Alberg, I.; Kramer, S.; Leps, C.; Tenzer, S.; Zentel, R. Effect of Core-Crosslinking on Protein Corona Formation on Polymeric Micelles. *Macromol. Biosci.* **2021**, *2000414*.

(66) Ojha, T.; Hu, Q.; Colombo, C.; Wit, J.; Geijn, M.; Steenbergen, M. J.; Bagheri, M.; Königs-Werner, H.; Buhl, E. M.; Bansal, R.; Shi, Y.; Hennink, W. E.; Storm, G.; Rijcken, C. J. F.; Lammers, T. Lyophilization Stabilizes Clinical-stage Core-crosslinked Polymeric Micelles to Overcome Cold Chain Supply Challenges. *Biotechnol. J.* **2021**, *16* (6), 2000212.

(67) Van Eerden, R. A. G.; Mathijssen, R. H. J.; Koolen, S. L. W. Recent Clinical Developments of Nanomediated Drug Delivery Systems of Taxanes for the Treatment of Cancer. *Int. J. Nanomedicine* **2020**, *15*, 8151–8166.

(68) Lee, Y. K.; Han, S. Y.; Chin, Y. W.; Choi, Y. H. Effects of Cysteine on the Pharmacokinetics of Paclitaxel in Rats. *Arch. Pharm. Res.* **2012**, *35* (3), 509–516.

(69) Galluzzi, L.; Senovilla, L.; Vitale, I.; Michels, J.; Martins, I.; Kepp, O.; Castedo, M.; Kroemer, G. Molecular Mechanisms of Cisplatin Resistance. *Oncogene* **2012**, *31* (15), 1869–1883.

(70) Gou, J.; Feng, S.; Xu, H.; Fang, G.; Chao, Y.; Zhang, Y.; Xu, H.; Tang, X. Decreased Core Crystallinity Facilitated Drug Loading in Polymeric Micelles without Affecting Their Biological Performances. *Biomacromolecules* **2015**, *16* (9), 2920–2929.

(71) Tyrrell, Z. L.; Shen, Y.; Radosz, M. Near-Critical Fluid Micellization for High and Efficient Drug Loading: Encapsulation of Paclitaxel into PEG-b-PCL Micelles. *J. Phys. Chem. C* **2011**, *115* (24), 11951–11956.

(72) Logie, J.; Ganesh, A. N.; Aman, A. M.; Al-awar, R. S.; Shoichet, M. S. Preclinical Evaluation of Taxane-Binding Peptide-Modified Polymeric Micelles Loaded with Docetaxel in an Orthotopic Breast Cancer Mouse Model. *Biomaterials* **2017**, *123*, 39–47.

(73) Huh, K. M.; Lee, S. C.; Cho, Y. W.; Lee, J.; Jeong, J. H.; Park, K. Hydrotropic Polymer Micelle System for Delivery of Paclitaxel. *J. Control. Release* **2005**, *101* (1-3 SPEC. ISS.), 59–68.

(74) Larsen, D.; Kietrys, A. M.; Clark, S. A.; Park, H. S.; Ekebergh, A.; Kool, E. T. Exceptionally Rapid Oxime and Hydrazone Formation Promoted by Catalytic Amine Buffers with Low Toxicity. *Chem. Sci.* **2018**, *9* (23), 5252–5259.

(75) Morales, S.; Aceña, J. L.; García Ruano, J. L.; Cid, M. B. Sustainable Synthesis of Oximes, Hydrazones, and Thiosemicarbazones under Mild Organocatalyzed Reaction Conditions. *J. Org. Chem.* **2016**, *81* (20), 10016–10022.

(76) Meel, R. Van Der; Sulheim, E.; Shi, Y.; Kiessling, F.; Mulder, W. J. M. Smart Cancer Nanomedicine. *Nat. Nanotechnol.* **2019**, *14* (November), 1007–1017.

(77) Alberg, I.; Kramer, S.; Schinnerer, M.; Hu, Q.; Seidl, C.; Leps, C.; Drude, N.; Möckel, D.; Rijcken, C.; Lammers, T.; Diken, M.; Maskos, M.; Morsbach, S.; Landfester, K.; Tenzer, S.; Barz, M.; Zentel, R. Polymeric Nanoparticles with Neglectable Protein

Corona. *Small* **2020**, *16* (18), 1907574.

(78) Rausch, K.; Reuter, A.; Fischer, K.; Schmidt, M. Evaluation of Nanoparticle Aggregation in Human Blood Serum. *Biomacromolecules* **2010**, *11* (11), 2836–2839.

(79) Shi, Y.; Van Nostrum, C. F.; Hennink, W. E. Interfacially Hydrazone Cross-Linked Thermosensitive Polymeric Micelles for Acid-Triggered Release of Paclitaxel. *ACS Biomater. Sci. Eng.* **2015**, *1* (6), 393–404.

(80) Bae, Y.; Nishiyama, N.; Fukushima, S.; Koyama, H.; Yasuhiro, M.; Kataoka, K. Preparation and Biological Characterization of Polymeric Micelle Drug Carriers with Intracellular PH-Triggered Drug Release Property: Tumor Permeability, Controlled Subcellular Drug Distribution, and Enhanced in Vivo Antitumor Efficacy. *Bioconjug. Chem.* **2005**, *16* (1), 122–130.

(81) Yardley, D. A. Nab-Paclitaxel Mechanisms of Action and Delivery. *J. Control. Release* **2013**, *170* (3), 365–372.

(82) Miele, E.; Spinelli, G. P.; Miele, E.; Tomao, F.; Tomao, S. Albumin-Bound Formulation of Paclitaxel (Abraxane ABI-007) in the Treatment of Breast Cancer. *Int. J. Nanomedicine* **2009**, *4*, 99–105.

(83) Kocere, A.; Resseguier, J.; Wohlmann, J.; Skjeldal, F. M.; Khan, S.; Speth, M.; Dal, N. K.; Ng, M. Y. W.; Alonso-Rodriguez, N.; Scarpa, E.; Rizzello, L.; Battaglia, G.; Griffiths, G.; Fenaroli, F. Real-Time Imaging of Polymersome Nanoparticles in Zebrafish Embryos Engrafted with Melanoma Cancer Cells: Localization, Toxicity and Treatment Analysis. *EBioMedicine* **2020**, *58*, 102902.

(84) Dal, N. K.; Kocere, A.; Wohlmann, J.; Van Herck, S.; Bauer, T. A.; Resseguier, J.; Bagherifam, S.; Hyldmo, H.; Barz, M.; De Geest, B. G.; Fenaroli, F. Zebrafish Embryos Allow Prediction of Nanoparticle Circulation Times in Mice and Facilitate Quantification of Nanoparticle–Cell Interactions. *Small* **2020**, *16* (5), 1906719.

Supporting Information

Experimental Section

Materials and Methods: Unless stated otherwise, solvents and reagents were used as received and purchased from Sigma-Aldrich. HFIP was purchased from Fluorochem, deuterated solvents were obtained from Deutero GmbH, (*R*)-lipoic and was bought from TCI Europe. PTX-LEV was obtained from Mercachem, Atto647N *N*-hydroxysuccinimide (NHS) was obtaind from Atto Tec GmbH. Tetrahydrofuran (THF) was dried over Na, chloroform ($CHCl_3$) was dried over CaH_2 and were freshly distilled before use. *N*,*N*-Diisopropylethylamine (DIPEA) and *N*,*N*-triethylamine (NEt_3) were dried over sodium hydroxide, distilled, and stored at -20 °C until further use. *N*,*N*-Dimethylformamide (DMF) (99.8 %, extra dry over molecular sieve) was bought from Acros and freshly freeze-pumped prior to use to remove residual dimethyl amine. MilliQ water was prepared by using a MILLI-Q Reference A+ System and used at a resistivity of 18.2 $M\Omega \cdot cm^{-1}$ and total organic carbon content below 5 ppm. Human blood plasma for DLS measurements was obtained from the Transfusion Center of the University Clinic of Mainz (Germany) from ten healthy donors after physical examination and after obtaining informed consent in accordance with the Declaration of Helsinki. The study was approved by the local ethics committee "Landesärztekammer Rheinland-Pfalz" (837.439.12 (8540-F)). All plasma batches were pooled and stored at -20 °C.

Atomic Force Microscopy: AFM was measured on Cypher (Asylum Research) or Dimension Icon (Bruker) AFMs in non-contact mode at a scan rate of 1 Hz. Samples were prepared by drop-casting of a particle solution (β = 50 $mg \cdot L^{-1}$ in water) onto freshly cleaned mica. The sample was dried overnight at room temperature. The AFM images were evaluated using Gwyddion 2.49.

Cryogenic Transmission Electron Microscopy: Cryo-EM images were recorded on a Talos L120C transmission electron microscope (Thermo Fisher Scientific) operating at 120 kV. The images were recorded at 13'500, 36'000, and 57'000-fold magnification. CCPMs (3.5 µL, β = 150 $mg \cdot L^{-1}$) were applied to freshly glow discharged Quantifoil® holey carbon films (R2/1 Cu 200, Quantifoil Micro Tools GmbH) and the grids were blotted for 2.5 s in a Vitrobot plunge-freezer (100% humidity, FEI Vitrobot Mark III, Thermo Fisher Scientific).

Single-Angle Dynamic Light Scattering: DLS measurements were performed on ZetaSizer Nano ZS or a Zetasizer Ultra (Malvern Panalytical Ltd.) equipped with a He-Ne laser (λ = 632.8 nm). All measurements were performed at 25 °C and a detection angle of 173° using disposable polystyrene cuvettes (VWR, Germany). Disposable folded capillary cells (Malvern Instruments Ltd.) were employed for ξ-potential measurements (3 mM sodium chloride). Cumulant size, polydispersity index (PDI), and size distribution histograms (intensity weighted) were calculated based on the autocorrelation function of the samples, with automated position and attenuator adjustments at multiple scans, and optional fluorescence filter.

Gel Permeation Chromatography: Gel permeation chromatography (GPC) was performed on a Jasco GPC setup at a flow rate of 1.0 mL·min^{-1} at 40°C using HFIP equipped with 3 g·L^{-1} of potassium trifluoroacetate as eluent and toluene as internal standard. GPC columns were purchased from PSS Polymer Standards Service GmbH (PFG-columns, particle size 7 µm, porosity 100 Å, 300 Å, and 4000 Å). Poly(methyl methacrylate) standards (PSS Polymer Standards Service GmbH) and pSar standards were used for calibration.[1] A UV detector (UV-4070, λ = 230 nm,) was used for polymer detection. Analysis was performed using PSS WinGPC (PSS Polymer Standards Service GmbH).

High Performance Liquid Chromatography: HPLC measurements were performed on a Beckman Coulter System Gold HPLC (Beckman Coulter, Inc), with a 508 autosampler, a 126 solvent module, a 168 detector, and a column oven equipped with a Luna C18(2) column (5µm, 100 Å, 250 × 4.6 mm) (Phenomenex LTD, Germany), controlled by the 32 Karat software (version 5.0, Beckman Coulter, Inc).

Infrared Spectroscopy: Attenuated total reflectance Fourier transform infrared (ATR-FT-IR) spectroscopy was performed on a FT/IR-4100 spectrometer (Jasco Corporation) with an ATR sampling accessory (MIRacle, Pike Technologies).

Multi-Angle Dynamic Light Scattering: For multi-angle DLS, cylindrical quartz cuvettes (Hellma, Mühlheim, Germany) were cleaned by dust-free distilled acetone and transferred to a dust free flow box. Light scattering measurements were performed on ALV spectrometers (ALV-5004 multiple-τ full digital correlator with He-Ne laser (632.8 nm) or ALV-CGS-3). The correlation functions of the particles were fitted using the sum of two exponentials. The z-average diffusion coefficient D_z was calculated by extrapolating D_{app} for q = 0. By formal application of Stokes law, the inverse z-average hydrodynamic radius is R_h=

$\langle R_h^{-1} \rangle_z^{-1}$ was determined. To investigate the aggregation behavior of the particles in human plasma, undiluted citrate plasma was filtered through a Millex GS 0.2 µm filter. The particle solutions were filtered through 0.2 µm pore size Millex GS filters. The following mixtures were prepared from initial particle solutions in 0.9% NaCl (ß = 30 g·L^{-1}): NaCl/particle solution 40:1 (ß = 0.75 g·L^{-1}), and plasma/particle solution 40:1 (ß = 0.75 g·L^{-1}). The cuvettes were incubated for 60 min at 37 °C before measurement at T = 20 °C. Data analysis was performed according to a procedure reported by Rausch *et al.*[2] The correlation functions of plasma were fitted with a triexponential decay function, and the particles were fitted using a sum of two exponentials. Mixtures were fitted using a sum of both exponential decay functions with or without additional aggregate term.

Nuclear Magnetic Resonance: All NMR spectra were recorded at room temperature on Avance II 400, Avance III 400, or Avance III 600 spectrometers (Bruker). Calibration of the spectra was achieved using the solvent signals and the spectra were analyzed with MestReNova 14.1.2 from Mestrelab Research S.L.

Polymer Synthesis: All polymers were synthesized by amine-initiated ring-opening NCA polymerization in dry DMF under a stream of dry N_2. The NCA monomers, sarcosine-NCA and *S*-ethylsulfonyl-L-cysteine-NCA were prepared as reported previously.[3,4]

Polysarcosine: The pSar macroinitiators were prepared following our procedure published previously.[5,6] Sarcosine-NCA (10.0 g; 86.9 mmol; 250 eq.) was weighed into a pre-dried Schlenk tube and dissolved in dry DMF (50 mL). Next, *N*-(*tert*-butoxycarbonyl)-1,2-diaminoethane (55.7 mg; 348 µmol; 1.0 eq.) was added as a stock solution in dry DMF. The reaction mixture was stirred at 10 °C in the absence of light until the reaction was completed, as monitored by FT-IR. The amine end-group was reacted with perfluorophenyl-4-azidobutanoate (205 mg; 695 µmol; 2.0 eq.) and DIPEA (296 µL; 1.74 mmol; 5.0 eq.). The reaction mixture was stirred overnight followed by addition of acetic anhydride (331 µL; 3.48 mmol; 10 eq.) and DIPEA (1.18 mL; 6.95 mmol; 20 eq.) to react with residual end-groups. The solution was stirred for one day at room temperature before the polymer was precipitated in acetone (800 mL), collected on a Buchner funnel, washed with acetone and diethyl ether, and dried *in vacuo*. Next, the Boc-group was removed. The polymer (5.50 g) was transferred to a round-bottom flask, dissolved in water (75 mL) and cooled to 0 °C. Trifluoro acetic acid (TFA) (75 mL) was added, and the solution was stirred at 0 °C for 5 h. Next, the solution was transferred into

dialysis bags (MWCO, 3.5 kDa) and dialyzed with water, sodium hydrogen carbonate solution, and water. The solution was lyophilized, and pSar (**P1**) was obtained as a colorless powder (4.20 g, 68%). Complete deprotection was confirmed by ^{1}H NMR, when the singlet of the Boc-group had vanished (1.37 ppm). The chain length was determined by HFIP-GPC relative to pSar standards (X_n = 200). For pSar with X_n > 250, the sarcosine NCA was added sequentially after monomer conversion was verified (120 eq. each).

^{1}H NMR (400 MHz, DMSO-*d*$_6$): δ (ppm) 4.49 - 3.77 (m, 2nH, -CH_2), 3.06−2.61 (m, 3nH, -CH_3).

Polysarcosine-block-Poly(S-ethylsulfonyl-L-cysteine): Block copolymers were prepared from pSar macroinitiators following the procedure published previously.[5,6] The pSar macroinitiator (**P1**) (2.08 g; 145 µmol; 1.0 eq.) was weighed into a Schlenk tube and dried by azeotropic distillation with toluene *in vacuo*. Next, pSar was dissolved in dry DMF (12 mL), cooled to -10 °C, and *S*-ethylsulfonyl-L-cysteine NCA (1.73 g; 7.25 mmol; 50 eq.) was added as a stock solution in dry DMF. The polymerization was performed at an NCA concentration of ß = 100 g·L^{-1} and monitored by FT-IR. After 5 days, no further reaction progress was observed (approx. 50%). The polymer was precipitated in THF, and the suspension was centrifuged (4500 rpm; 5 min; 4 °C) and decanted. The procedure was repeated twice, concluding with diethyl ether. The product was dried *in vacuo* yielding pSar$_{200}$-*b*-p(L)Cys(SO_2Et)$_{27}$ (**P3**) as a colorless solid (2.57 g, 74%). For dye labeling, the polymer (**P3**, 58 mg; 2.91 µmol; 1.0 eq.) was dissolved in 1.5 mL of DMSO and Atto647N-*N*-hydroxysuccinimide (3.69 mg; 4.37 µmol; 1.5 eq.) was added from a stock solution in DMSO (ß = 10 g·L^{-1}; 369µL), and the solution was stirred at room temperature for 48 h. The unconjugated dye was removed by repetitive precipitation in THF (4500 rpm, 3 min, 4°C) and the polymer was dried *in vacuo*. Absence of free dye was verified by HFIP-GPC. ^{1}H NMR (400 MHz, DMSO-*d*$_6$): δ (ppm) 8.77 (b s, 1mH, CON*H*), 4.68 (m, 1mH, α-C$H_{(L\text{-}Cys)}$), 4.49 - 3.78 (m, 2nH, -C$H_{2(Sar)}$), 3.55 (m, 4mH, -S-CH_2, -SO_2-CH_2), 3.06 - 2.61 (m, 3nH, -$CH_{3(Sar)}$), 1.29 (t, 3mH, -$CH_{3(L\text{-}Cys)}$).

Cross-Linker Synthesis:

(R)-Methyl Lipoate: (*R*)-Methyl lipoate (**2**) was synthesized according to our previous publication, following a modified procedure from Hassan and Maltman.[6,7] (*R*)-Lipoic acid (**1**) (1.00 g; 4.85 mmol; 1.0 eq.) was dissolved in dry methanol (10 mL), and a catalytic amount of sulfuric acid (2.58 µL; 48.5 µmol;

0.01 eq.) was added. The reaction mixture was stirred at room temperature for 18 h in the absence of light. Next, methanol was removed *in vacuo* and the crude was dissolved in dichloromethane (DCM). The organic phase was washed with saturated $NaHCO_3$ solution (3x) and brine (3x), dried over $MgSO_4$, filtered, and concentrated *in vacuo*. (*R*)-Methyl lipoate (**2**) was obtained as a yellow oil (0.90 g, 84%) and used without further purification. ^{1}H NMR (400 MHz, $CDCl_3$): δ (ppm) 3.67 (s, 3H, -OC*H*$_3$), 3.57 (m, 1H, -S-C*H*), 3.15 (m, 2H, -S-C*H*$_2$), 2.47 (m, 1H, -S-CH$_2$-C*H*$_2$), 2.33 (t, *J* = 7.5 Hz, 2H, α-C*H*$_2$), 1.91 (m, 1H, -S-CH$_2$-C*H*$_2$), 1.73–1.61 (m, 4H, ß-C*H*$_2$, δ-C*H*$_2$), 1.49 (m, 2H, γ-C*H*$_2$).

^{13}C NMR (101 MHz, $CDCl_3$): δ (ppm) 174.1, 56.5, 51.7, 40.4, 38.6, 34.8, 34.0, 28.9, 24.8.

(R)-Lipoic Acid Hydrazide: (*R*)-Lipoic acid hydrazide (**3**) was synthesized according to our previous publication, following a modified procedure from Koufaki *et al.*[6,8] (*R*)-Methyl lipoate (**2**) (895 mg; 4.04 mmol; 1.0 eq.) was dissolved methanol (8 mL), and hydrazine hydrate (1.19 mL; 24.3 mmol; 6.0 equiv) was added. The reaction mixture was stirred at room temperature for 72 h shielded from light. The solution was concentrated *in vacuo* and dissolved in ethyl ethanoate. The organic layer was washed with brine (5x), dried with $MgSO_4$, filtered, and concentrated *in vacuo*. (*R*)-Lipoic acid hydrazide (**3**) was obtained as a yellow oil (630 mg, 71%) and used without further purification. ^{1}H NMR (400 MHz, $CDCl_3$): δ (ppm) 6.71 (b s, 1H, -CON*H*), 3.56 (m, 1H, -S-C*H*), 3.15 (m, 2H, -SC*H*$_2$), 2.46 (m, 1H, -S-CH$_2$C*H*$_2$), 2.16 (t, *J* = 7.3 Hz, 2H, α-C*H*$_2$), 1.91 (m, 1H, -S-CH$_2$C*H*$_2$), 1.77-1.59 (m, 4H, -ß-C*H*$_2$, δ-C*H*$_2$), 1.55-1.39 (m, 2H, γ-C*H*$_2$). ^{13}C NMR (101 MHz, $CDCl_3$): δ (ppm) 173.7, 56,5, 40.4, 38.6, 34.7, 34.4, 29.0, 25.3. ESI-MS (*m*/*z* = 243.20): $[M + Na]^+$; $[M+Na]^+$ (calc.), 243.06 g·mol^{-1}.

Synthesis of PTX-LEV-LA: (*R*)-Lipoic acid hydrazide (**3**) (27.8 mg; 126 µmol; 3.0 eq.) was dissolved in a mixture of absolute MeOH (200 µL) and dry $CHCl_3$ (200 µL). Next, paclitaxel-levulinic acid (PTX-LEV) (40.0 mg; 42.0 µmol; 1.0 eq.) was added and the flask was equipped with three beads of activated molecular sieve 3A and the reaction mixture was stirred at room temperature. After full conversion of PTX-LEV (3 days), as monitored by TLC, the solvents were removed with a stream of dry nitrogen and the crude product was purified by column chromatography (dichloromethane + 5 vol.% EtOH) yielding PTX-LEV-LA (**4**) as a yellow solid (36.2 mg; 3.14 µmol; 75%).

ESI-MS (m/z = 1176.4187 $[M+Na]^+$; $[M+Na]^+$ (calc.) 1176.4168 g·mol^{-1}).

The structure was confirmed by NMR analysis, whereby coexisting rotamers were observed by NOESY.

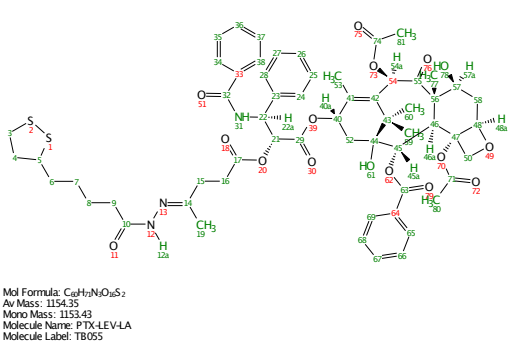

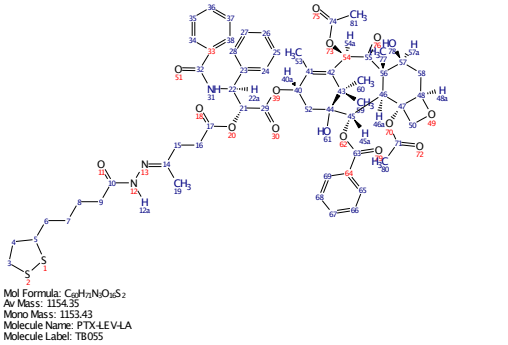

cis-Rotamer (green numbering):

^{1}H NMR (600 MHz, DMSO-d_6): δ (ppm) = 9.98 (s, 1H, 12a), 9.19 (s, 1H, 31), 7.97 (m, 2H, 65, 69), 7.82 (m, 2H, 34, 38), 7.74 (m, 1H, 67), 7.67 (m, 2H, 66, 68), 7.48 (m, 7H, 24, 25, 27, 28, 35, 36, 37), 7.17 (m, 1H, 26), 6.27 (s, 1H, 54a), 5.79 (m, 1H, 40a), 5.45 (t, J_{HH} = 9.1 Hz, 1H, 22a), 5.40 (dd, J_{HH} = 12.8, 7.2 Hz, 1H, 45a), 5.27 (dd, J_{HH} =8.6, 2.6 Hz, 1H, 21), 4.91 (m, 2H, 48a, 78), 4.62 (s, 1H, 61), 4.09 (m, 1H, 57a), 4.00 (m, 2H, 50), 3.56 (m, 3H, 5, 46a), 3.12 (m, 2H, 3), 2.62 (m, 2H, 16), 2.55 (m, 2H, 15), 2.40 (m, 3H, 4', 9), 2.25 (s, 3H, 80), 2.10 (s, 3H, 81), 1.84 (m, 1H, 4"), 1.76 (s, 3H, 53), 1.72 (s, 3H, 19), 1.70 - 1.50 (m, 8H, 6, 8, 52, 58), 1.48 (s, 3H, 77), 1.40 - 1.30 (m, 2H, 7), 1.01 (d, J_{HH} = 4.5 Hz, 1H, 60), 0.99 (d, J_{HH} = 3.7 Hz, 1H, 61);

trans-Rotamer (blue numbering):

^{1}H NMR (600 MHz, DMSO-d_6): δ (ppm) = 10.29 (d, J_{HH} = 3.2 Hz, 1H, 12a), 9.30 (dd, J_{HH} = 8.3 Hz, 3.1 Hz, 1H, 31), 7.97 (m, 2H, 65, 69), 7.82 (m, 2H, 34, 38), 7.74 (m, 1H, 67), 7.67 (m, 2H, 66, 68), 7.48 (m, 7H, 24, 25, 27, 28, 35, 36, 37), 7.17 (m, 1H, 26), 6.27 (s, 1H, 54a), 5.79 (m, 1H, 40a), 5.56 (t, J_{HH} = 8.6 Hz, 1H, 22a), 5.40 (dd, J_{HH} = 12.8, 7.2 Hz, 1H, 45a), 5.23 (d, J_{HH} = 10.0, 1H, 21), 4.91 (m, 2H, 48a, 78), 4.62 (s, 1H, 61), 4.09 (m, 1H, 57a), 4.00 (m, 2H, 50), 3.56 (m, 3H, 5, 46a), 3.12 (m, 2H, 3), 2.62 (m, 2H, 16), 2.55 (m, 2H, 15), 2.40 (m, 1H, 4'), 2.30 (m, 2H, 9), 2.25 (s, 3H, 80), 2.10 (s, 3H, 81), 1.84 (m, 4H, 4", 19), 1.76 (s, 3H, 53), 1.70 - 1.50 (m, 8H, 6, 8, 52, 58), 1.48 (a, 3H, 77), 1.40 - 1.30 (m, 2H, 7), 1.01 (d, J_{HH} = 4.5 Hz, 1H, 60), 0.99 (d, J_{HH} = 3.7 Hz, 61).

Perfluorophenyl (R)-5-(1,2-dithiolan-3-yl)pentanoate: Perfluorophenyl (*R*)-5-(1,2-dithiolan-3-yl)pentanoate (**5**) was synthesized according to our previous publication.[5] (*R*)-Lipoic acid (**1**) (4.00 g; 19.4 mmol; 1.0 eq.) was weighed into a dry Schlenk flask and dissolved in dry THF (10.0 mL) at room temperature. Next, DIPEA (3.96 mL; 23.3 mmol; 1.2 eq.) and pentafluorophenyl trifluoroacetate (4.00 mL; 23.3 mmol; 1.2 eq.) were added with a counterflow of dry N_2 and the reaction mixture was stirred for 48 h at room temperature in the absence of light. The solvent was concentrated *in vacuo* and the crude product was purified by column chromatography (cyclohexane/ethyl ethanoate; 9/1 to 7/1) yielding perfluorophenyl (*R*)-5-(1,2-dithiolan-3-yl)pentanoate (**5**) as a yellow oil (6.73 g; 18.1 mmol; 93%). ^{1}H NMR (300 MHz, $CDCl_3$) δ (ppm) = 3.59 (m, 1H, -SC*H*), 3.16 (m, 2H, -S-C*H*$_2$), 2.69 (t, *J* = 7.3 Hz, 2H, α-C*H*$_2$), 2.47 (m, 1H, -S-CH$_2$-*CH*$_2$), 1.93 (m, 1H, -S-CH$_2$-*CH*$_2$), 1.87 - 1.69 (m, 4H, ß-C*H*$_2$, δ-C*H*$_2$), 1.69 - 1.47 (m, 2H, γ-C*H*$_2$). ^{19}F NMR (282 MHz, $CDCl_3$) δ (ppm) = -154.0 (m), -159.2 (t) , -163.5 (m). FD-MS (m/z = 372.2847 $[M]^+$; $[M]^+$ (calc.) 372.0272 g·mol^{-1}).

(R)-5-(1,2-Dithiolan-3-yl)-N-(naphthalen-1-ylmethyl)pentanamide: Perfluorophenyl (*R*)-5-(1,2-dithiolan-3-yl)pentanoate (**5**) (1.17 g; 3.14 mmol; 1.0 eq.) was weighed in a pre-dried Schlenk-flask, dissolved in absolute DCM (12 mL) and cooled to 0 °C. Next, NEt_3 (1.32 mL; 9.43 mmol; 3.0 eq.) and naphthalen-1-ylmethanamine (592 mg; 3.77 mmol; 1.2 eq.) were added, and the reaction mixture was allowed to reach room temperature. A colorless solid precipitated after 30 minutes. After 24 h, the solid was removed by filtration. The filtrate was diluted with DCM and washed with 10% $NaHCO_3$ solution (5x) and brine (3x). The organic phase was dried with $MgSO_4$, filtered, and concentrated *in vacuo*. To remove pentafluorophenol, the crude yellow oil was placed in a water bath (40 °C) and connected to high vacuum for 5 h. The crude product was purified by column chromatography (DCM + 2% MeOH) yielding (*R*)-5-(1,2-dithiolan-3-yl)-*N*-(naphthalen-1-ylmethyl)pentanamide (**6**) as a yellow solid (800 mg; 2.32 mmol; 74%). ^{1}H NMR (400 MHz, $CDCl_3$): δ (ppm) = 8.00 (m, 1H, -C$_{8,\,arom.}$-*H*), 7.85 (m, 2H, -C$_{5,\,arom.}$-*H*, -C$_{4,\,arom.}$-*H*), 7.54 (m, 2H, -C$_{6,\,arom.}$-*H*, C$_{7,\,arom.}$-*H*), 7.44 (m, 2H, -C$_{1,\,arom.}$-*H*, -C$_{2,\,arom.}$-*H*), 5.69 (m, 1H, -N*H*), 4.91 (d, *J* = 5.3 Hz, 2H, -NH-C*H*$_2$), 3.52 (m, 1H, -S-C*H*), 3.13 (m, 2H, -S-C*H*$_2$), 2.42 (m, 1H, -S-CH$_2$-C*H*$_2$), 2.20 (t, *J* = 7.3 Hz, 2H, α-C*H*$_2$), 1.86 (m, 1H, -S-CH$_2$-C*H*$_2$), 1.80 - 1.60 (m, 4H, ß-C*H*$_2$, δ- C*H*$_2$), 1.55 - 1.34 (m, 2H, γ-C*H*$_2$). ESI-MS (m/z = 346.1221 $[M+H]^+$; M^+ (calc.) 345.1294 g·mol^{-1}).

CCPMs by Self-Assembly: The preparation of core cross-linked polymeric micelles (CCPMs) was adapted from our previous publications and modified by the use of

DMSO.[5,6] The polypept(o)ide, $pSar_{200}$-*b*-p(L)$Cys(SO_2Et)_{17}$ (**P1**), was dissolved in DMSO equipped with 1 M thiourea at a concentration of 7.5 $g \cdot L^{-1}$. After 1 h, 20 vol.% 1 mm acetate buffer (pH 4.75) equipped with 10 mm thiourea was added, and the solution was left to equilibrate at room temperature for 3 h, followed by dialysis against 1 mm acetate buffer (pH 4.75) containing 10 mM thiourea. The solution was filtered (PVDF 450) and concentrated to approx. 7 $g \cdot L^{-1}$ by spin filtration (Amicon Ultra; MWCO, 3 kDa), yielding the micelle solution. For cross-linking, (*R*)-lipoic acid hydrazide (**3**) was dissolved in ethanol at a concentration of $\beta = 20\ g \cdot L^{-1}$ in a separate flask, and one equivalent of tris(2-carboxyethyl)phosphine hydrochloride (TCEP·HCl) ($\beta = 50\ g \cdot L^{-1}$ in water) was added. After reaction overnight, the cross-linker solution was added to the micelle solution at equimolar amounts of thiols per cysteines. The reaction mixture was stirred at room temperature for at least 48 h. To remove thiourea, residual cross-linker and unconjugated polymer, the solution was dialyzed against DMSO and water mixtures (1/1 and 100% water) (MWCO, 6–8 kDa) followed by spin filtration (Amicon Ultra; MWCO, 100 kDa). The absence of the free polymer was verified by HFIP-GPC.

CCPMs by Continuous Flow Process: CCPMs were created in a three-step process, consisting of 1) the self-assembly of polymeric micelles, 2) the cross-linking of polymeric micelles and 3) the purification and concentration of the product solution. The first two steps were prepared by fluidic mixing over a SIMM V2 micromixer produced by Fraunhofer IMM. In preparation of the reaction, two reaction fluids were prepared. For the polymer solution, 450 mg of the polypept(o)ide, $pSar_{200}$-*b*-p(L)$Cys(SO_2Et)_{17}$ were dissolved in 60 mL of DMSO, leading to a clear solution after 30 min. To this solution, 18 mL of water were added, and the mixture was left to equilibrate for another 30 min. The total concentration of the polypept(o)ide was thus 5.7 $g \cdot L^{-1}$. For the cross-linker solution, 49,5 mg of (*R*)-lipoic acid hydrazide was dissolved in 40 mL of ethanol and 20 mL water. To this solution, one equivalent of tris(2-carboxyethyl)phosphine hydrochloride (TCEP·HCl) in 18 mL water was added and left to react for 2 h, leading to a clear solution. The concentrations of polymer and cross-linker in their respective solutions were prepared to ensure full conversion of the polymer when applying an equal volume of cross-linker solution. For the micelle preparation, the polymer solution was combined with water over a micromixer. Generally, the delivery of the reagent solutions was done by HPLC pumps with subsequent backpressure valves. All pumps were under regular

inspection to ensure reproducible flowrates. The total flowrate was kept at 10 mL·min^{-1}, the individual flowrates were adjusted to achieve a 1/10 or 1/5 dilution. The first 10 mL of the produced micelle solution were recovered before the process stream was switched into the second stage. Here, a volume stream of cross-linker solution equivalent to the polymer solution stream was added. No intermediate clean-up was performed. The product solution was then forwarded to a tangential flow filtration system for downstream processing.

Downstream processing via TFF: Before entering the membrane system, the product stream was diluted by an additional stream of 30 mL·min^{-1} of deionized water. The combined stream was fed over a regenerated cellulose membrane with an average porosity of 30 kDa. With an outlet stream of 3 mL·min^{-1} on retentate side and 37 mL·min^{-1} on permeate side. After completing the reaction, the TFF membrane was flushed with 15 mL of deionized water with closed permeate line to recover the remaining particles between the membranes. In total the unreacted polymer as well as crosslinker and organic solvents in the product stream were reduced by >90 % and the concentration of CCPMs was increased 3-fold. For higher purification, a discontinuous procedure was added. In this approach, the product solution was diluted with an aliquot of water and then fed through the TFF system maintaining a permeate-to-retentate ratio of 3 to 1. The recovered retentate was re-fed to the original solution while the permeate was continuously removed until the total volume of raw product is reduced to one tenth of its original volume. After this step, the solution was diluted with additional water; the cycle was then repeated until HFIP-GPC didn't show any leftover unreacted polymer.

PTX Conjugation in DMSO: CCPMs (3.05 mg; 0.15 µmol copolymer; 2.23 µmol hydrazide-CL; 1.0 eq.) were weighed into an Eppendorf tube, dissolved in dry DMSO (500 µL), and PTX-LEV (0.64 mg; 0.67 µmol; 0.3 eq. per hydrazide-CL) was added from a stock solution in dry DMSO. The reaction mixture was placed on a benchtop shaker at 50°C for 7 days. The reaction mixture was transferred to a dialysis bag (3.5 kDa, MWCO) and dialyzed against water. The white precipitate was separated by centrifugation (4500 rpm, 5 min, 20 °C) and the supernatant was collected, filtered (PVDF; 220 nm), and lyophilized. The particles were weighed (2.68 mg; 73% yield) and reconstituted in sterile water at a concentration of 30 g·L^{-1}.

PTX Conjugation by Film-Hydration: CCPMs (10.0 mg; 0.49 µmol copolymer; 7.30 µmol hydrazide-CL; 1.0 eq.) were placed into a 50 mL round bottom flask and PTX-LEV (2.0 mg; 2.19 µmol; 0.3 eq. per hydrazide-CL) was added from a stock solution in EtOH. The reaction mixture was placed in a water bath for 1 h (50 °C) before the solvent was removed *in vacuo*. The particles were re-suspended with water (3 mL) and ethanol (7 mL) and dried *in vacuo* once more. Subsequently, the particles were reconstituted in water at a concentration of 1 $g \cdot L^{-1}$, the white precipitate was separated by centrifugation (4500 rpm, 5 min, 20 °C) and the supernatant was collected, filtered (PVDF; 220 nm), and lyophilized. The particles were weighed (9,35 mg; 78% yield) and reconstituted in sterile water at a concentration of 30 $g \cdot L^{-1}$.

PTX Quantification and Release: The PTX content was determined by RP-HPLC using an external calibration (PTX-LEV; 8.450 min; UV-detector, λ = 230 nm) with gradient mixtures of water (+ 0.1 vol.% TFA) and acetonitrile (ACN) as mobile phase at a flow rate of 1 $mL \cdot min^{-1}$: 60% ACN for 1 min, increase to 85% ACN over 8 minutes, hold at 85% for 5 min, decrease to 60% ACN in 1 min. PTX@CCPM solutions were analyzed in buffer (β_{CCPM} = 1 $g \cdot L^{-1}$) containing 20 mm NH_4OAc, 134 mM NaCl, and 1.0 vol.% Tween 80 (pH 5.0). Samples (50 µL) were diluted with ACN (550 µL) and filtered (PTFE, 220 nm) before analysis. To determine the amount of non-conjugated drug, samples were taken immediately after mixing. For total drug content, the solution was additionally equipped with 10 mM TCEP, and the sample was taken after incubation for 24 h. For release studies, PTX@CCPMs were incubated in buffer at pH 5.0 (20 mM NH_4OAc, 134 mM NaCl, 1.0 vol.% Tween 80) or pH 7.4 (PBS, 1.0 vol.% Tween 80). Aliquots were taken at: 1 min, 0.5 h, 1.5 h, 3 h, 7 h, 17 h, 24 h, and 48 h. The PTX release was calculated based on the total PTX content, and data were taken from 3 independent experiments.

Cell Culture: HeLa cells (CCL-2) and B16F1 cells were cultured in their respective medium (DMEM/PenStrep/Glutamine) at 37 °C and 5 % CO_2 and were handled under sterile working conditions. They were subcultured every 3 days. To determine the viable cell count, cells were counted using a Casy TTC Cell (OLS). Cells were seeded in 96well plates at a density of 6,000 cells/well and treated for the indicated time spans 24 h post-seeding. For IC_{50} evaluations, cells were treated for 48 h. Viability was assayed 48 h after start of treatment using CellTiter-Glo® 2.0 Viability Assay according to the manufacturer's instructions. Luminescence readings were performed on a Tecan Spark® (Tecan) and signal

intensities normalized to untreated control samples incubated under the same conditions. Further analysis and plotting was performed on GraphPad PRISM.

In Vivo Experiments in Zebrafish Larvae:

Zebrafish Handling and Care: Zebrafish embryos were maintained in petri dishes containing zebrafish egg water supplemented with 0.003% phenythiourea (PTU). The petri dishes were kept in an incubator at a stable temperature of 28.5 °C. A maximum of 20 zebrafish embryos were placed in each dish which contained no less than 20 mL of egg water. All experiments were performed in accordance with the ethical standards and legislation for animal research in Norway (License FOTS-ID: 13563).

Circulation Time Analysis in Zebrafish: To evaluate the stability of CCPMs in the blood circulation of zebrafish the protocol described in Dal *et al.* was used.[9] Briefly, a pipette puller (P-97, Sutter Instrument) was used to produce borosilicate needles for injections. The needle was mounted on a micromanipulator (Narishige MN-153) connected to an Eppendorf FemtoJet express pump. Before injections, zebrafish were sedated in a tricaine bath (Finquel; 0.02% in zebrafish egg water) and placed on a plate containing hardened agarose gel (2% in water). Two-day old zebrafish embryos were injected in the posterior cardinal vein with 5 nL of CCPM solution. At defined times (5 min, 1 h, 4 h, and 24 h) an image of the whole zebrafish (30X magnification) and of the caudal region (120X magnification) was acquired using a Leica DFC365FX stereo microscope with a 1.0X plan apo lens.

The average fluorescence of the artery (AF, 30X), normalized by the average total fluorescence of the zebrafish (TF, 120X), was used to determine the nanoparticle circulation in the blood flow. The average artery fluorescence at 5 minutes (AF-5min) was considered as 100% meaning that all nanoparticles were considered in circulation at this time point. The values obtained were subtracted by the background fluorescence analyzed in zebrafish injected with PBS. The final analysis was therefore performed as follows:

$$\text{CCPM circulation, \%} = \frac{\frac{\text{AF-time x}}{\text{TF-time x}}\text{background}}{\frac{\text{AF-5 min}}{\text{TF-5 min}}\text{background}} * 100\%$$

CCPM Accumulation in Zebrafish: Mouse melanoma B16 cells expressing RFP (pGIPZ-RFP lentiviral vector) were used. The cells were grown at 37°C in RPMI-1640 medium (Lonza, Switzerland) with 10% FBS (Saveen & Werner, Norway)

puromycin (2 µg/mL, Sigma-Aldrich, USA). Cancer cells were detached using Versene (Life Technologies, USA) and centrifuged at 400 relative centrifugal force to obtain a cell pellet that was used to load borosilicate needles for subsequent zebrafish injections. Three-day old zebrafish embryos were xenotransplanted in the neural tube with approx. 200 B16F1 cells. After this, zebrafish embryos were kept in petri dishes in an incubator at 32 °C. After 5 days, treatment (PTX@CCPMs, ABX) or control (CCPMs, PBS) were injected in the posterior cardinal vein. To determine the nanoparticle accumulation in the tumor region, and an image of the zebrafish was taken after 8 hours at 30X using a Leica DFC365FX stereomicroscope with a 1.0X plan apo lens, and images were analyzed using the software Fiji.

Toxicity Analysis in Zebrafish: Zebrafish embryos were injected in the posterior cardinal vein at day 3 post fertilization with varying amounts of PTX@CCPMs or ABX. CCPMs and PBS were used as controls. The survival of zebrafish embryos in each treatment group was analyzed up to day 5 post injection.

Tumor Therapy in Zebrafish: Three-day old zebrafish embryos were injected in the neural tube with approx. 200 mouse melanoma B16F1 cells expressing RFP. After 24 h, the zebrafish embryos were divided into four groups each receiving one of the following treatments by injection in the posterior cardinal vein: 1. Abraxane, 5 ng of PTX; 2. PTX@CCPM, 10 ng of PTX; 3. CCPMs (control); 4. PBS (control). Six days later, images were recorded for each zebrafish (30X magnification) using a Leica DFC365FX stereomicroscope with a 1.0X plan apo lens, and images were analyzed using Fiji.

Data Management and Statistical Analysis: Data sets were managed using Microsoft Excel (Microsoft Corporation, USA), Graph Pad Prism (GraphPad Software, USA), and MagicPlot Student 2.9.3. For statistical analysis, differences between individual were evaluated by two-way ANOVA, and were considered significant for $p < 0.05$ (*$p < 0.05$, **$p < 0.01$, ***$p < 0.001$, ****$p < 0.0001$).

Results and Discussion

Polymer Synthesis

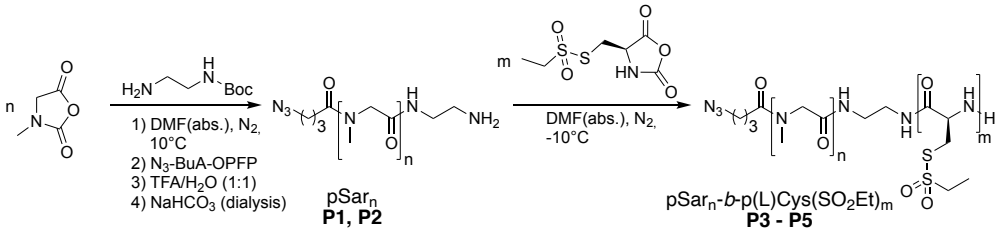

Scheme S1. Scheme of the polypept(o)ide synthesis by ring-opening NCA polymerization according to Klinker *et al.* and Bauer *et al.*[5,6]

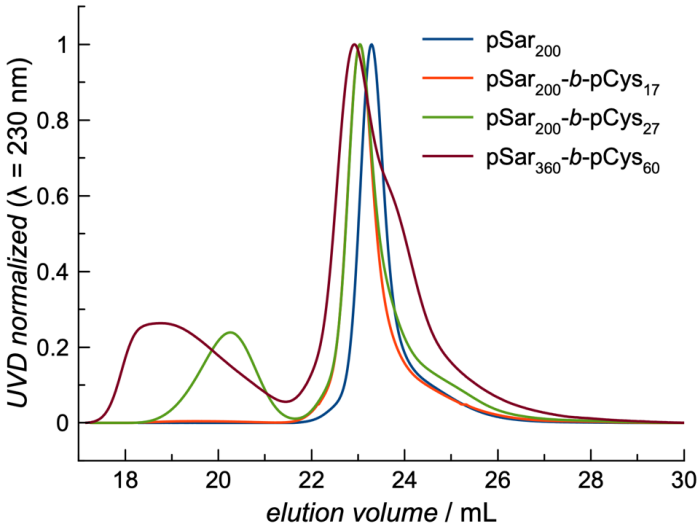

Figure S1. Analytical HFIP-GPC of polypept(o)ides. Note that secondary structure formation (anti-parallel ß-sheet) is not suppressed in HFIP accounting for the broad PDI of copolymers with increasing chain length of p(L)Cys(SO_2Et).[10,11]

Table S1. Characterization of core cross-linked polymeric micelles with and without embedded iron oxide nanoparticles.

polymer	X_n pSar[a]	X_n pCys(SO_2Et)[b]	M_n[c]	*yield*	$Đ$[c]
P1	200	-	36.6 kg·mol^{-1}	4.20 g	1.17
P2	360	-	38.3 kg·mol^{-1}	0.55 g	1.23

P3	200	17	40.6 kg·mol^{-1}	2.30 g	1.19
P4	200	27	40.3 kg·mol^{-1}	2.57 g	4.65
P5	360	60	45.1 kg·mol^{-1}	0.53 g	8.52

[a] HFIP-GPC relative to pSar standards. [b] determined by ^{1}H NMR. [c] HFIP-GPC relative to PMMA standards; note that secondary structure formation of p(L)Cys(SO2Et) is not suppressed, which induces aggregation accounting for multimodal GPC elugrams and broad dispersities.

Cross-Linker Synthesis

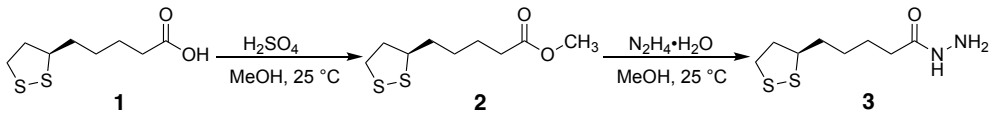

Scheme S2. Chemical reaction pathway to (*R*)-lipoic acid hydrazide (**3**) starting from (*R*)-lipoic acid (**1**), according to Bauer *et al.*[6]

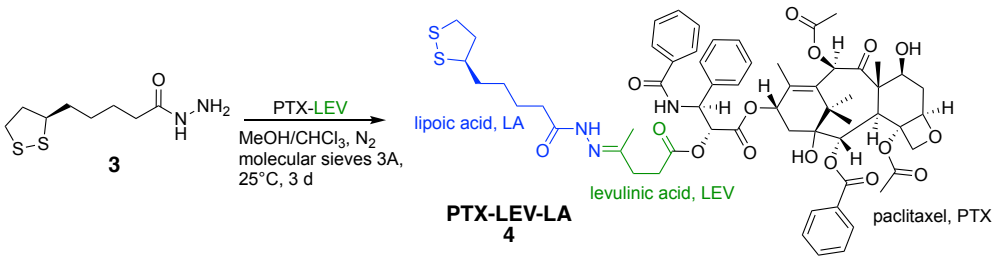

Scheme S3. Chemical reaction pathway to functional cross-linker PTX-LEV-LA (**4**).

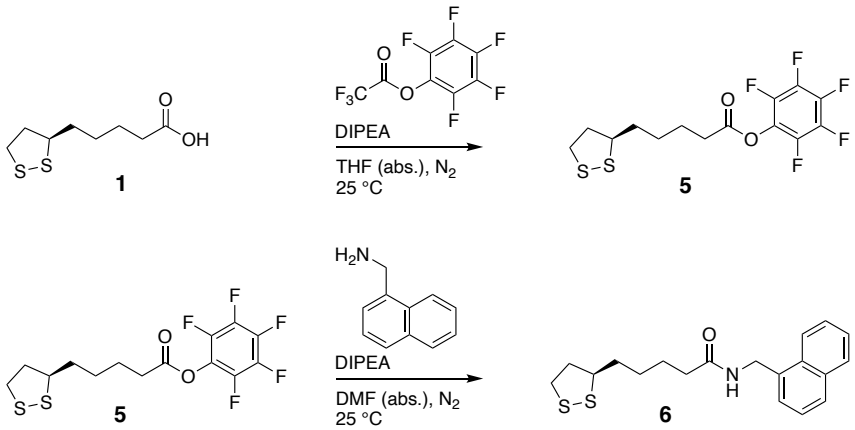

Scheme S4. Chemical reaction pathway to (*R*)-5-(1,2-dithiolan-3-yl)-*N*-(naphthalen-1-ylmethyl)pentanamide (**6**) via perfluorophenyl (*R*)-5-(1,2-dithiolan-3-yl)pentanoate (**5**). The procedure was adapted and modified from Klinker *et al.*[5]

Core Cross-Linked Polymeric Micelles

Particle Synthesis by Micromixer

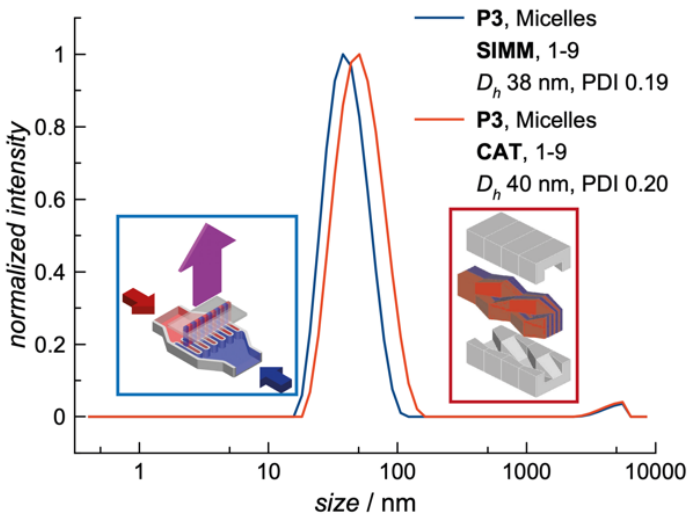

Figure S2. DLS analysis of polymeric micelles by micromixer: influence of the micromixer. Polymeric micelles could be successfully generated from slit interdigital micromixers (SIMM) and caterpillar micromixers (CAT) at asymmetric flow rates of 1 to 9 and optimal overall flow rates of 10 mL·min^{-1}. Lower overall flow rates lead to polydisperse samples, and pulsation effects are observed beyond 20 mL·min^{-1}. Despite only minor differences were detected for CAT and SIMM at entirely optimized conditions in DLS, SIMM offered easier handling and reduced tendency to form aggregates. The SIMM was therefore chosen in the following for self-assembly and cross-linking.

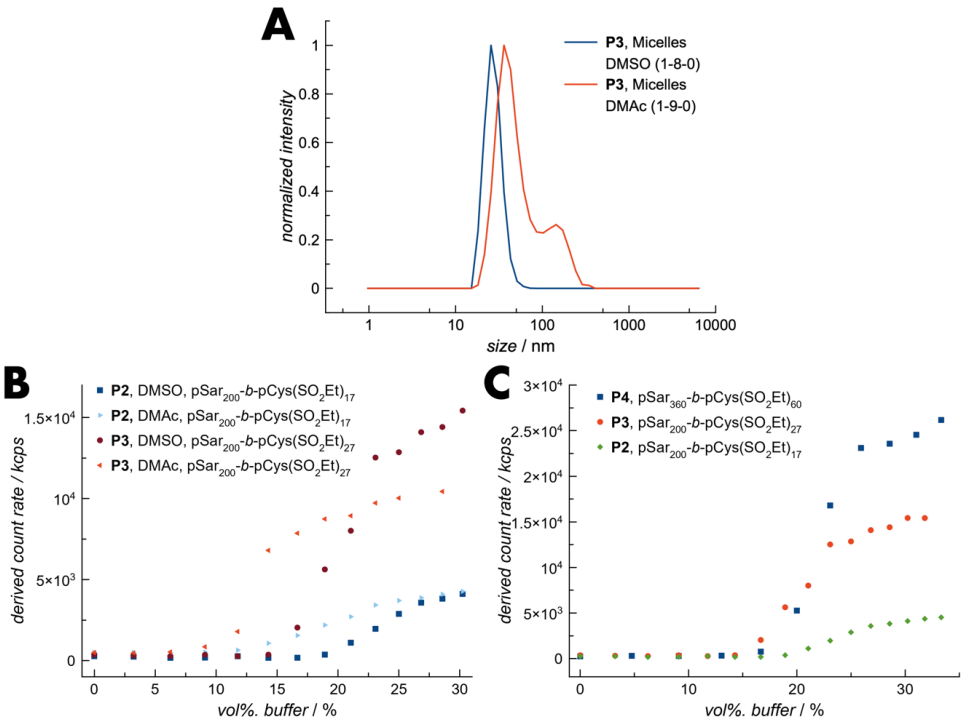

Figure S3. DLS analysis of polymeric micelles by micromixer: influence of the solvent. (**A**) Micelles formed via micromixer from **P3** using DMAc or DMSO. DMSO leads to more uniform particles due to the better solubility of the copolymer. (**B**) Aggregation curve of **P2** and **P3** in DMSO or DMAc. The aggregation in DMSO starts at higher buffer content, indicating better solubility of the copolymer. (**C**) Aggregation curve of **P2**, **P3** and **P4** in DMSO. Higher pCys(SO_2Et) fractions lead to earlier aggregation.[6]

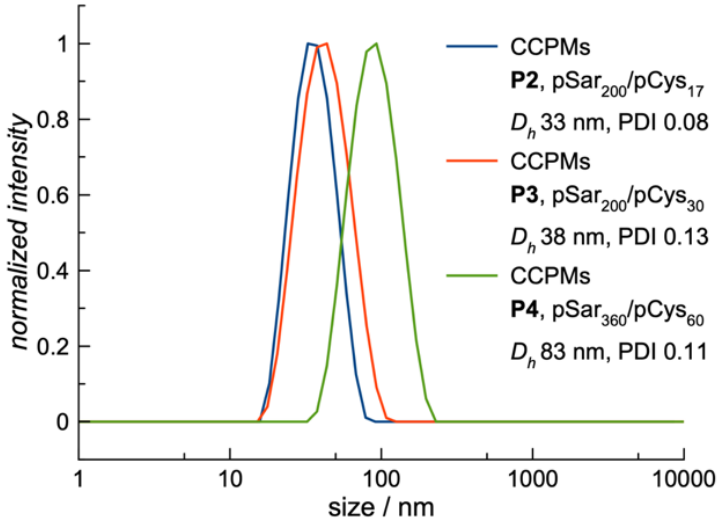

Figure S4. DLS analysis of CCPMs by micromixer: influence of the chain length. CCPM size increases for increasing block lengths of pSar$_n$-*b*-pCys(SO$_2$Et)$_m$ with n = 200 or 360 and m = 17, 30, and 60 (**P2**, **P3**, **P4**).

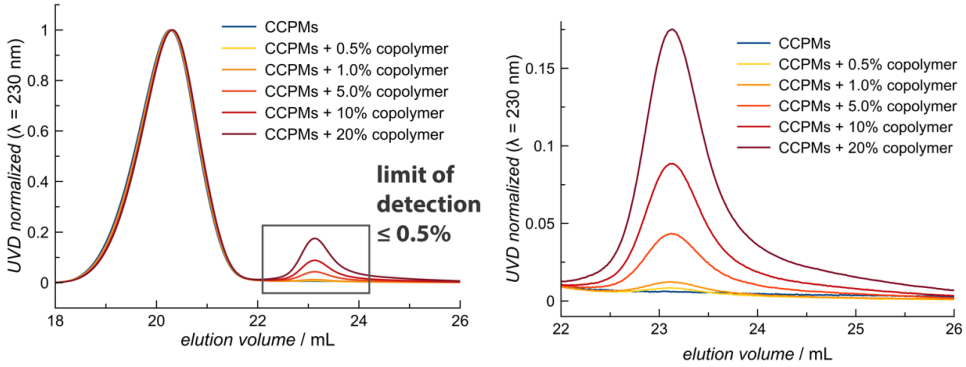

Figure S5. HFIP-GPC analysis: Determining the limit of detection. Contaminations as low as 0.5% copolymer can be detected.

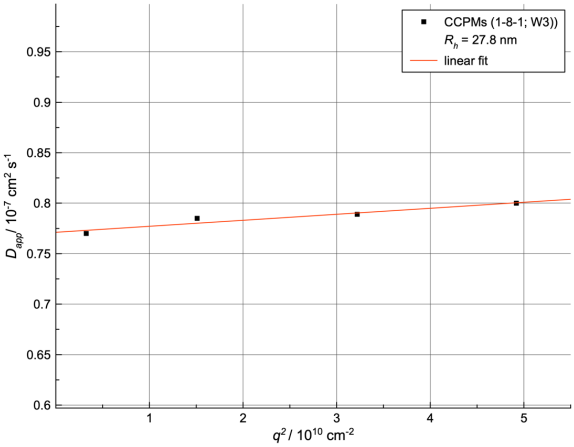

Figure S6. Multi-angle DLS analysis of micromixer CCPMs after purification by cross-flow filtration. A hydrodynamic diameter of 27.8 nm was derived from the bi-exponential fit of the autocorrelation curve, whereby only a slight angle-dependency could be detected for measurements at 26°, 58°, 90°, and 122°.

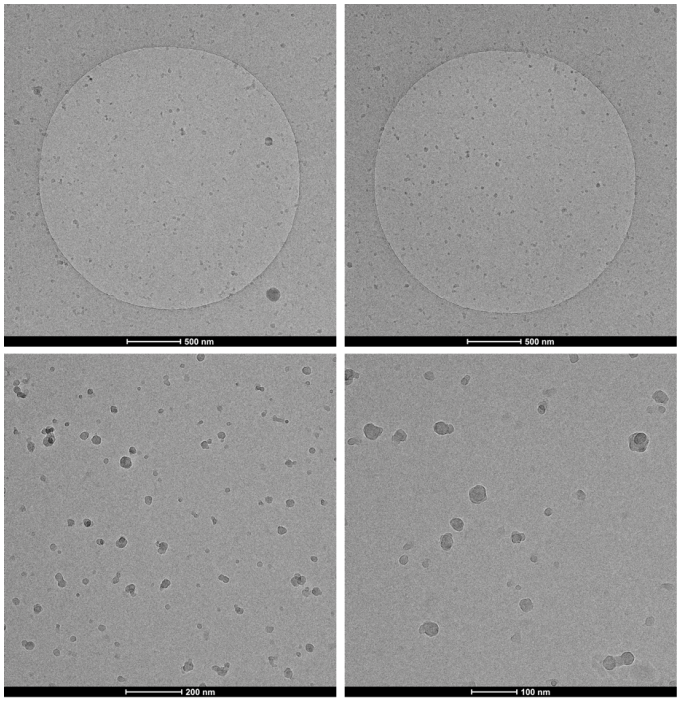

Figure S7. CryoTEM images of CCPMs produced by micromixer (1-8-1; W3).

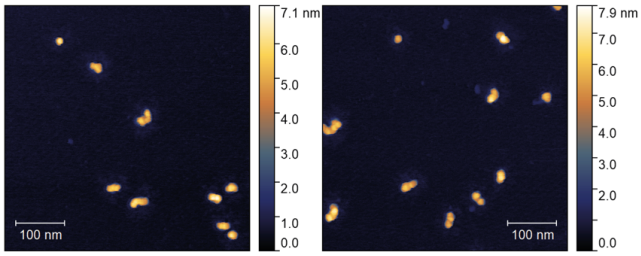

Figure S8. Additional AFM images of CCPMs produced by micromixer (1-8-1; W3).

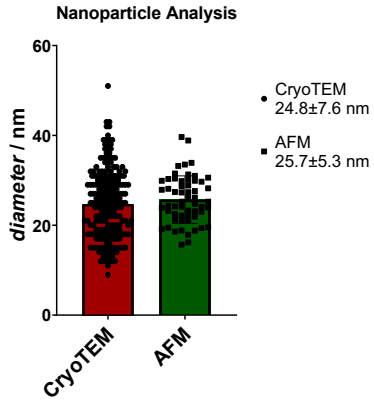

Figure S9. Particle size of micromixer-CCPMs (1-8-1; W3) as determined by CryoTEM and AFM image analysis.

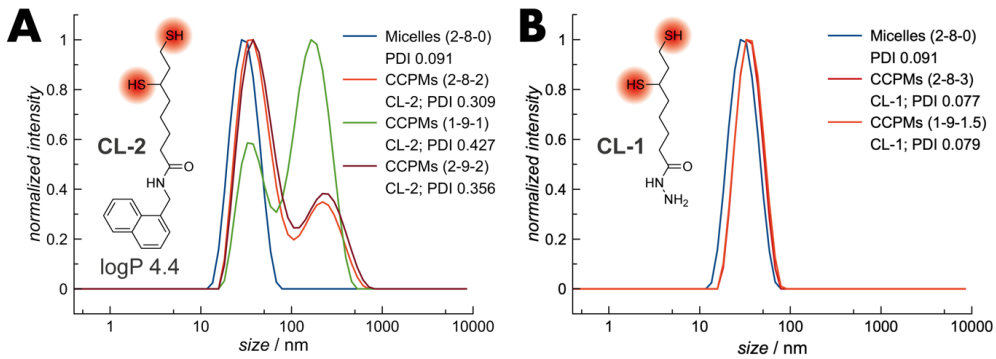

Figure S10. DLS analysis of CCPMs by micromixer: influence of the cross-linker. (**A**) Micelle cross-linking with the hydrophobic cross-linker (*R*)-5-(1,2-dithiolan-3-yl)-*N*-(naphthalen-1-ylmethyl)pentanamide (**6**) leads to aggregate formation (turbid solutions, multimodal size distribution in DLS) irrespective of the cross-linking flow rates. (**B**) Micelle cross-linking with the functional (*R*)-lipoic acid hydrazide (**3**) leads to CCPMs with

monomodal distribution and narrow PDI and is not affected by the applied volume flow ratios.

Cross-Linking by Pro-Drug Drug Cross-Linker (PTX-LEV-LA)

Applying the functional pro-drug cross-linker PTX-LEV-LA (**4**) leads to turbid particle solutions, whereby the particle structure cannot be preserved. Moreover, only low drug contents of 0.9 wt.% can be determined (encapsulation efficiency < 1%), which are not sufficient for stabilization by core cross-linking. Furthermore, low reaction yields do not justify the synthetic effort.

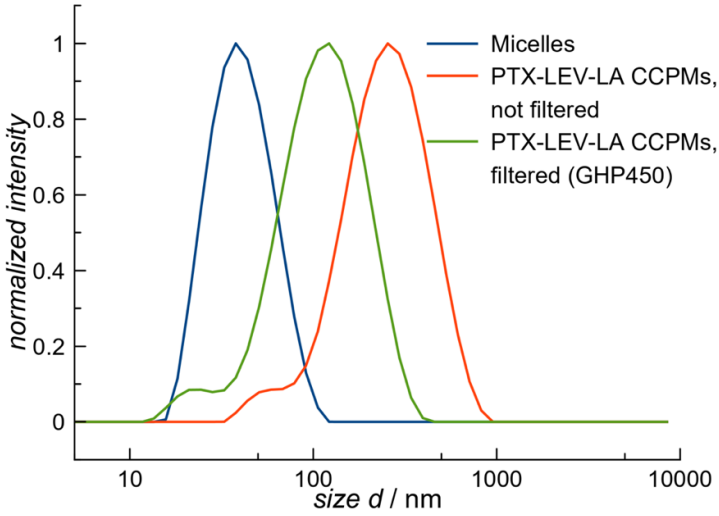

Figure S11. Dynamic light scattering of micelles before and after cross-linking with PTX-LEV-LA (**4**).

PTX-LEV Conjugation

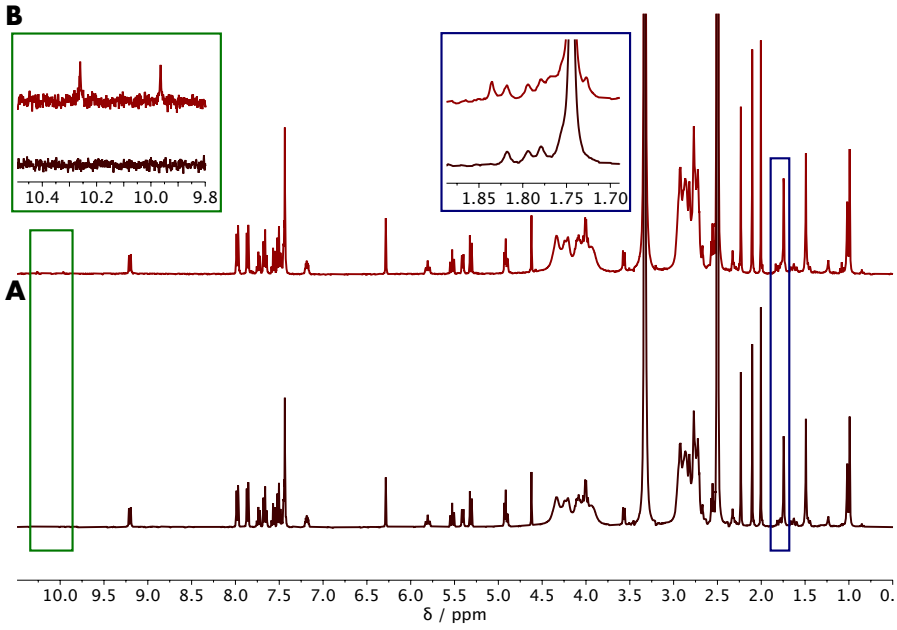

Figure S12. 1H NMR analysis of the PTX-LEV conjugation to lipoic acid hydrazide-functionalized CCPMs in DMSO-d_6. (**A**) CCPMs + PTX-LEV at t = 0 h. (**B**) CCPMs + PTX-LEV at t = 7 days. Significant peaks at 10.3/9.95ppm and 1.84 ppm account for hydrazone-bond formation: Green box: C=O-N*H*-N=CR'(CH_3); Blue box: -N=CR'(CH_3).

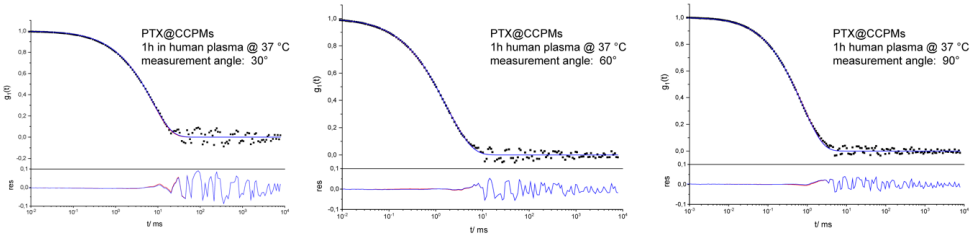

Figure S13. Multi angle DLS of PTX@CCPMs in undiluted human plasma: Autocorrelation function $g_1(t)$ given for the measurement angles of 30°, 60°, and 90°. The fits with (blue line) and without (red line) aggregation term (upper graph), and derived residuals for the fit w/o aggregate and correlation function indicate no significant aggregation (lower graph).

Cell Culture

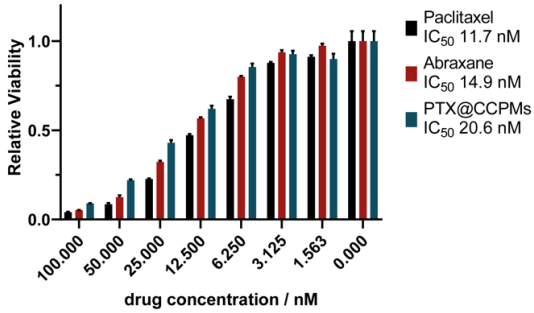

Figure S14. Analysis of PTX@CCPMs, Abraxane, and free PTX in HeLa cells. IC_{50} values were calculated for 100 µM as maximal inhibition show comparable performance of the three paclitaxel formulations.

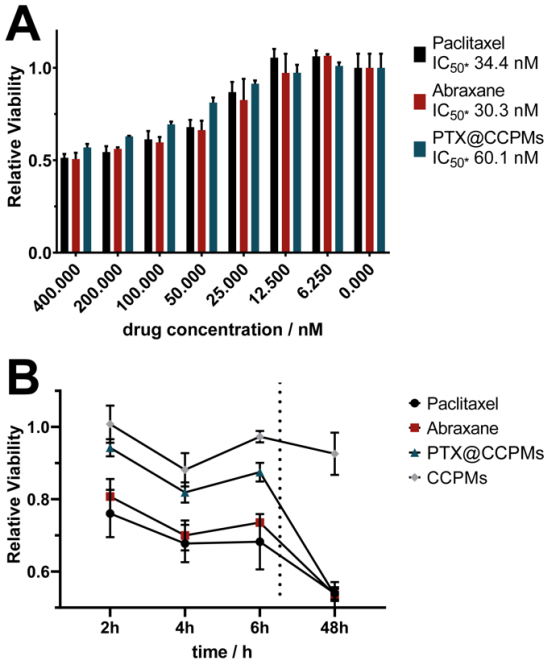

Figure S15. Analysis of PTX@CCPMs, Abraxane, and free PTX in B16F1 cells. (**A**) IC_{50} values were calculated for 400 µM as maximal inhibition. (**B**) Time-dependent toxicity of PTX formulations at 100 µM.

In vivo experiments

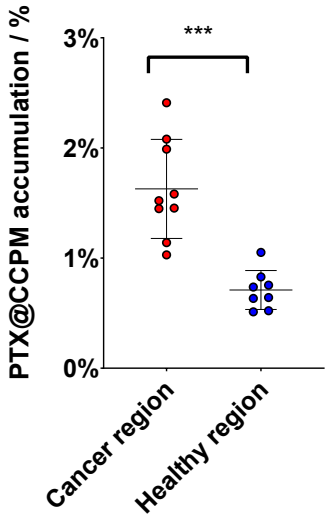

Figure S16. Tumor accumulation of PTX@CCPMs at 8 h post nanoparticle administration. Accumulation values based on nanoparticle fluorescence at t = 5 min (100% in circulation). According to Figure S17, more than 40% are expected to be still in circulation.

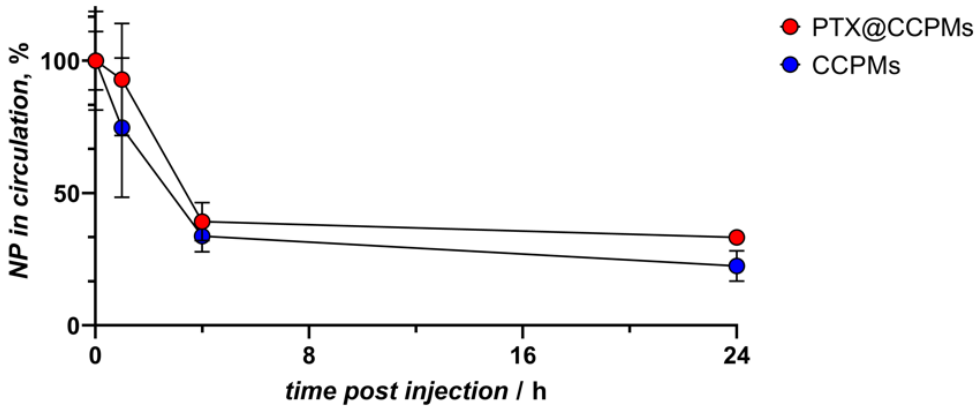

Figure S17. Circulation time analysis of PTX@CCPMs and CCPMs in zebrafish embryo.

References for Supporting Information

(1) Weber, B.; Birke, A.; Fischer, K.; Schmidt, M.; Barz, M. Solution Properties of Polysarcosine: From Absolute and Relative Molar Mass Determinations to Complement Activation. *Macromolecules* **2018**, *51* (7), 2653–2661.

(2) Rausch, K.; Reuter, A.; Fischer, K.; Schmidt, M. Evaluation of Nanoparticle Aggregation in Human Blood Serum. *Biomacromolecules* **2010**, *11* (11), 2836–2839.

(3) Birke, A.; Huesmann, D.; Kelsch, A.; Weilbächer, M.; Xie, J.; Bros, M.; Bopp, T.; Becker, C.; Landfester, K.; Barz, M. Polypeptoid- Block -Polypeptide Copolymers: Synthesis, Characterization, and Application of Amphiphilic Block Copolypept(o)Ides in Drug Formulations and Miniemulsion Techniques. *Biomacromolecules* **2014**, *15* (2), 548–557.

(4) Schäfer, O.; Huesmann, D.; Muhl, C.; Barz, M. Rethinking Cysteine Protective Groups: S -Alkylsulfonyl- l -Cysteines for Chemoselective Disulfide Formation. *Chem. - A Eur. J.* **2016**, *22* (50), 18085–18091.

(5) Klinker, K.; Schäfer, O.; Huesmann, D.; Bauer, T.; Capelôa, L.; Braun, L.; Stergiou, N.; Schinnerer, M.; Dirisala, A.; Miyata, K.; Osada, K.; Cabral, H.; Kataoka, K.; Barz, M. Secondary-Structure-Driven Self-Assembly of Reactive Polypept(o)Ides: Controlling Size, Shape, and Function of Core Cross-Linked Nanostructures. *Angew. Chemie Int. Ed.* **2017**, *56* (32), 9608–9613.

(6) Bauer, T. A.; Imschweiler, J.; Muhl, C.; Weber, B.; Barz, M. Secondary Structure-Driven Self-Assembly of Thiol-Reactive Polypept(o)Ides. *Biomacromolecules* **2021**, *22* (5), 2171–2180.

(7) Hassan, H. M. A.; Maltman, B. A. Mixed SAMs and MALDI-ToF MS: Preparation of N-Glycosylamine Derivative and Thioctic Acid Methyl Ester Bearing 1,2-Dithiolane Groups and Detection of Enzymatic Reaction on Au. *Bioorg. Chem.* **2012**, *40* (1), 6–9.

(8) Koufaki, M.; Kiziridi, C.; Alexi, X.; Alexis, M. N. Design and Synthesis of Novel Neuroprotective 1,2-Dithiolane/Chroman Hybrids. *Bioorg. Med. Chem.* **2009**, *17* (17), 6432–6441.

(9) Dal, N. K.; Kocere, A.; Wohlmann, J.; Van Herck, S.; Bauer, T. A.; Resseguier, J.; Bagherifam, S.; Hyldmo, H.; Barz, M.; De Geest, B. G.; Fenaroli, F. Zebrafish Embryos Allow Prediction of Nanoparticle Circulation Times in Mice and Facilitate Quantification of Nanoparticle–Cell Interactions. *Small* **2020**, *16* (5), 1906719.

(10) Bauer, T. A.; Muhl, C.; Schollmeyer, D.; Barz, M. Racemic S -(Ethylsulfonyl)- Dl -cysteine N -Carboxyanhydrides Improve Chain Lengths and Monomer Conversion for B-Sheet-Controlled Ring-Opening Polymerization. *Macromol. Rapid Commun.* **2021**, *42* (8), 2000470.

(11) Bauer, T. A.; Horvat, N. K.; Marques, O.; Chocarro, S.; Mertens, C.; Colucci, S.; Schmitt, S.; Carrella, L. M.; Morsbach, S.; Koynov, K.; Fenaroli, F.; Blümler, P.; Jung, M.; Sotillo, R.; Hentze, M. W.; Muckenthaler, M. U.; Barz, M. Core Cross-Linked Polymeric Micelles for Specific Iron Delivery: Inducing Sterile Inflammation in Macrophages. *Adv. Healthc. Mater.* **2021**, *10* (19), 2100385.

Appendix

NMR Spectroscopy

Cross-Linker Syntheses

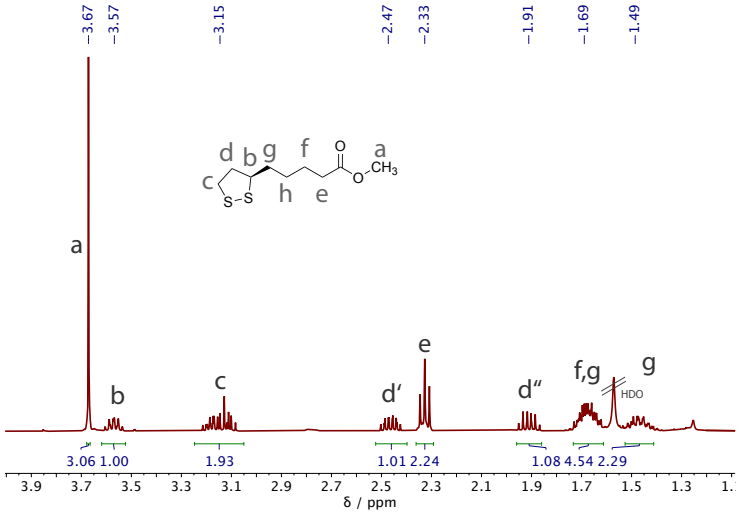

Figure S18. ^{1}H NMR Analysis of (*R*)-methyl liponamide (**2**) in $CDCl_3$.

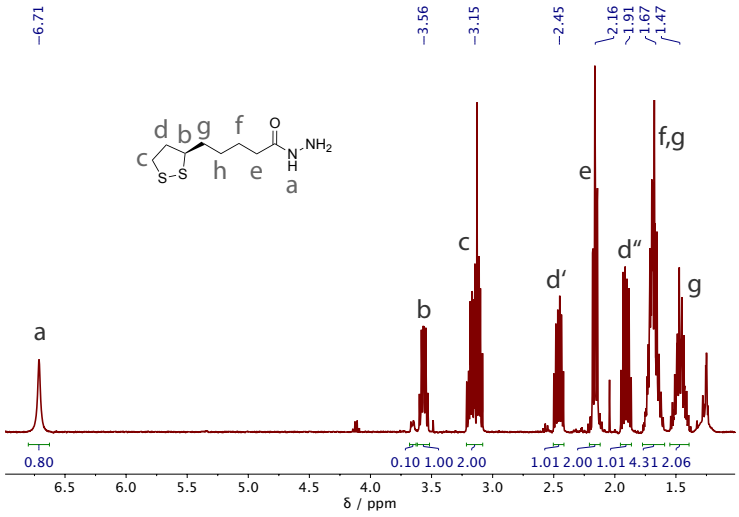

Figure S19. ^{1}H NMR Analysis of (*R*)-lipoic acid hydrazide (**3**) in $CDCl_3$.

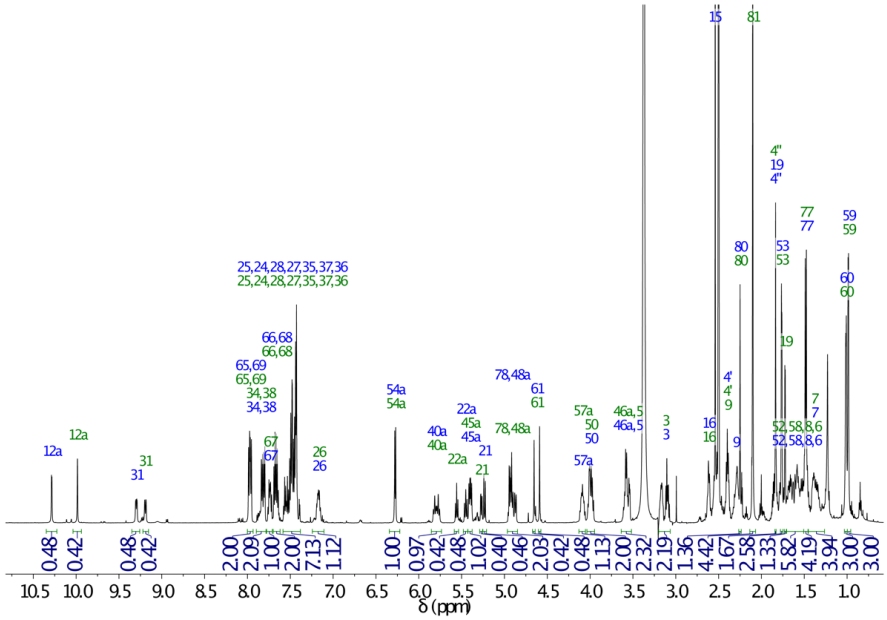

Figure S20. ^{1}H NMR analysis of PTX-LEV-LA (**4**) in DMSO-d_6.

Assignment for PTX-LEV-LA:

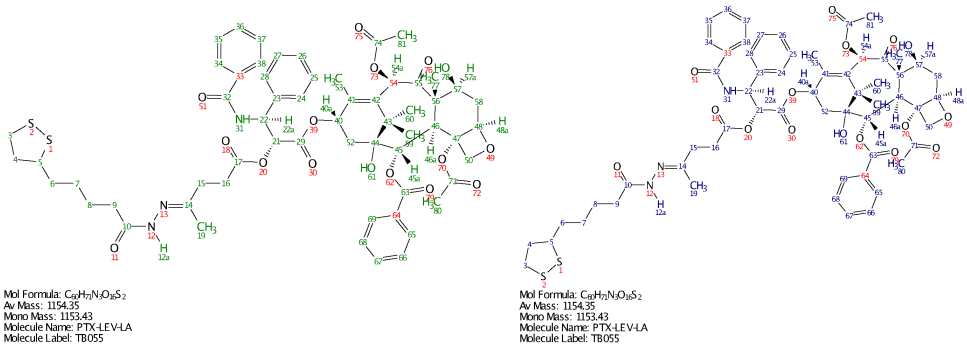

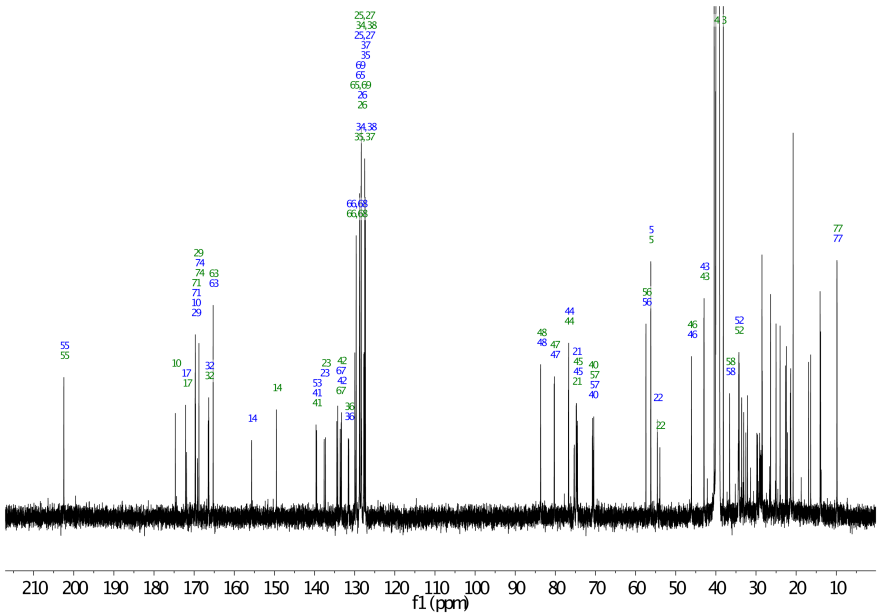

Figure S21. ^{13}C NMR analysis of PTX-LEV-LA (**4**) in DMSO-d_6.

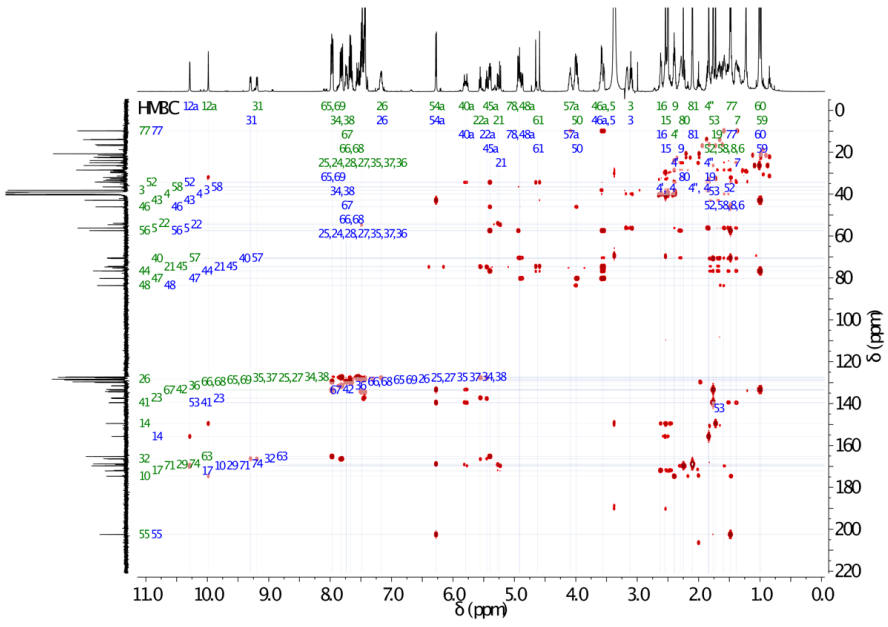

Figure S22. $^{1}H,^{13}C$ HMBC analysis of PTX-LEV-LA (**4**) in DMSO-d_6.

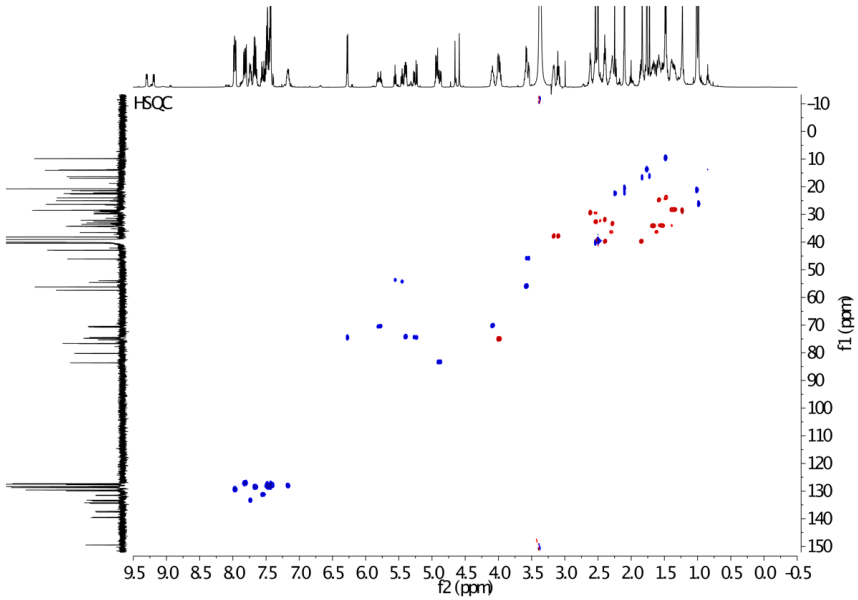

Figure S23. ^{1}H, ^{13}C HSQC analysis of PTX-LEV-LA (**4**) in DMSO-d_6.

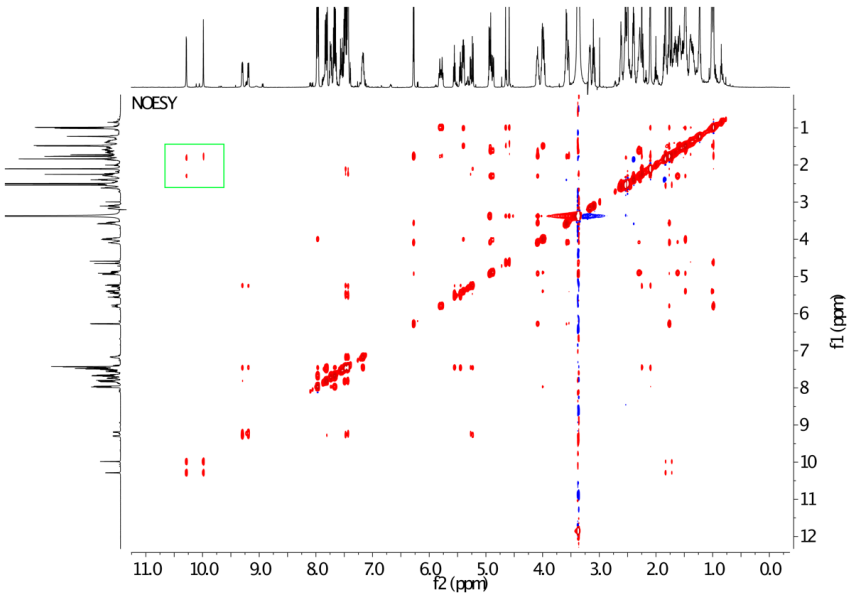

Figure S24. ^{1}H NOESY analysis of PTX-LEV-LA (**4**) DMSO-d_6. The green box indicates different coupling between *cis*- and *trans*-rotamers of PTX-LEV-LA (**4**).

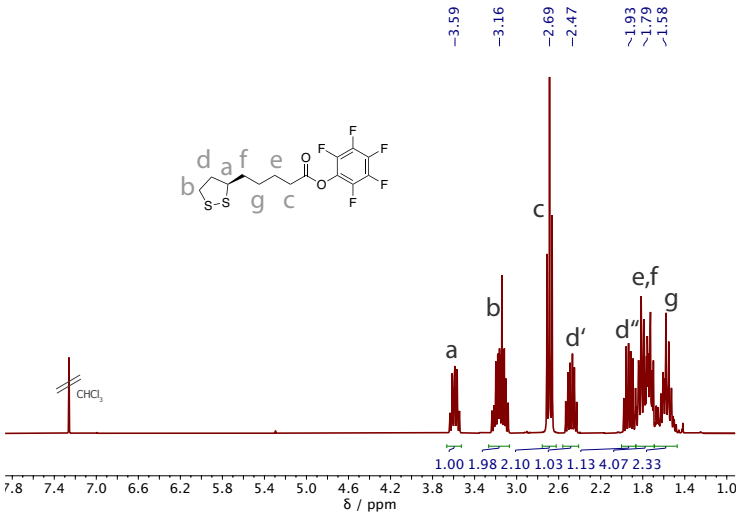

Figure S25. ^{1}H NMR Analysis of perfluorophenyl (*R*)-5-(1,2-dithiolan-3-yl)pentanoate (**5**) in $CDCl_3$.

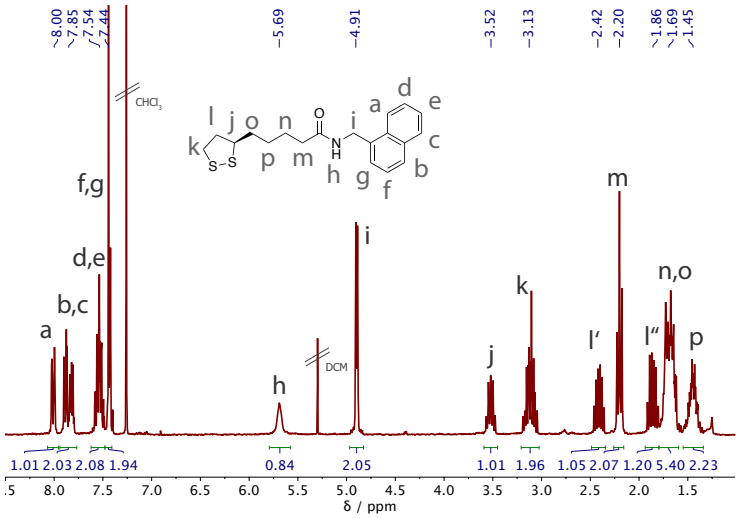

Figure S26. ^{1}H NMR Analysis of (*R*)-5-(1,2-dithiolan-3-yl)-*N*-(naphthalen-1-ylmethyl)pentanamide (**6**) in $CDCl_3$.

Polypept(o)ides

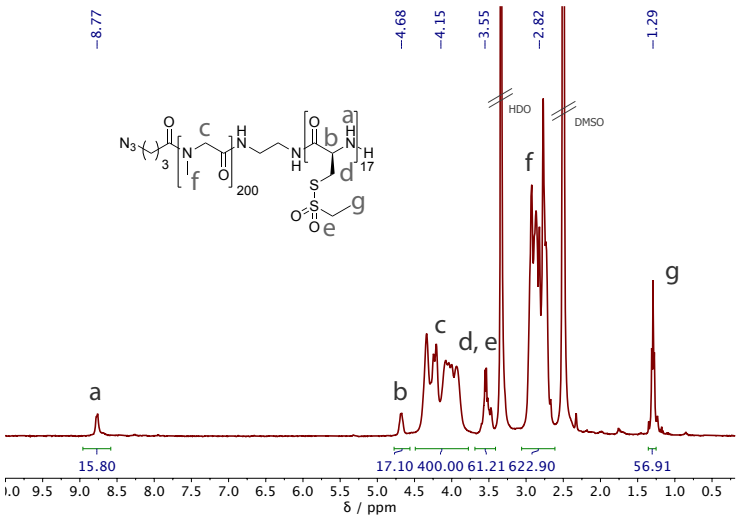

Figure S27. ^{1}H NMR Analysis of pSar$_{200}$-*b*-p(L)Cys(SO$_2$Et)$_{17}$ in DMSO-d_6.

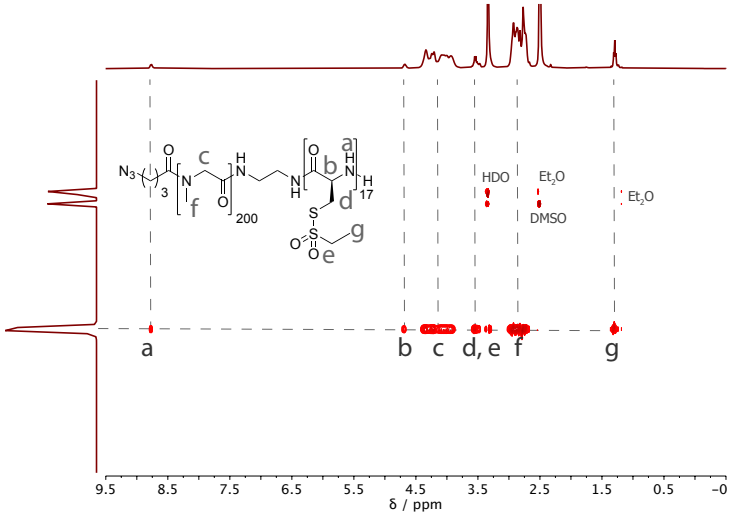

Figure S28. DOSY NMR Analysis of pSar$_{200}$-*b*-p(L)Cys(SO$_2$Et)$_{17}$ in DMSO-d_6.

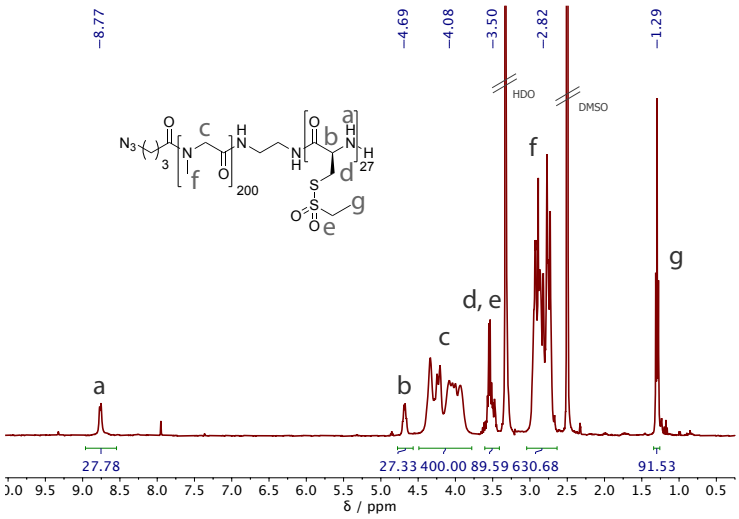

Figure S29. ^{1}H NMR Analysis of pSar$_{200}$-*b*-p(L)Cys(SO$_2$Et)$_{27}$ in DMSO-d_6.

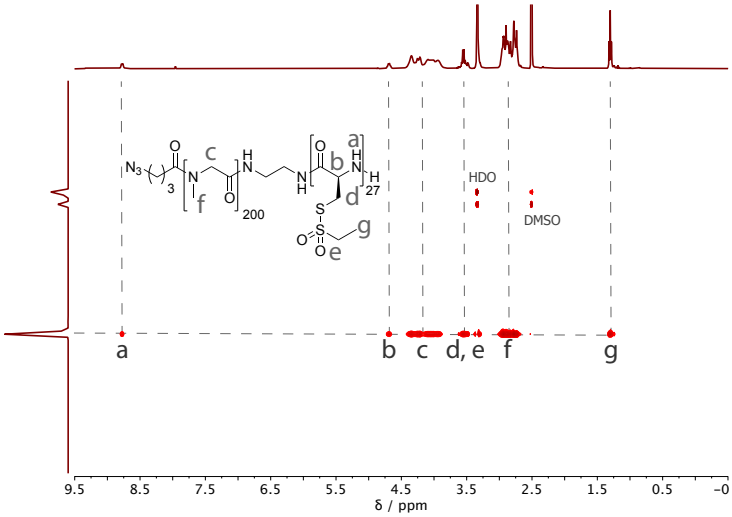

Figure S30. DOSY NMR Analysis of pSar$_{200}$-*b*-p(L)Cys(SO$_2$Et)$_{27}$ in DMSO-d_6.

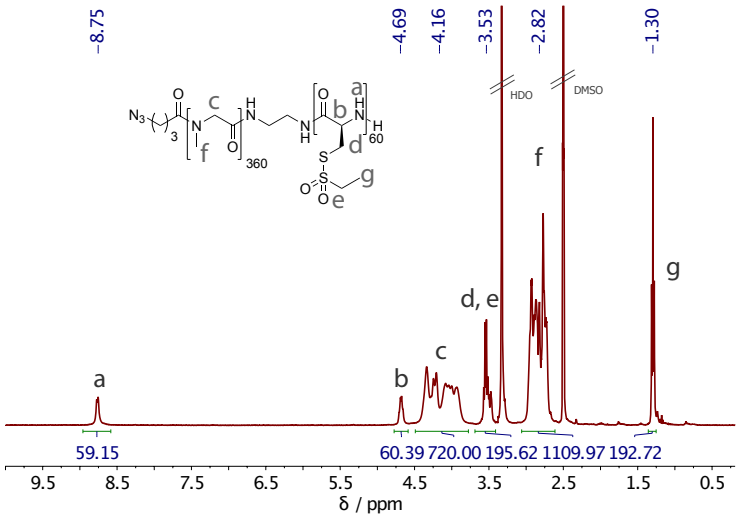

Figure S31. ^{1}H NMR Analysis of pSar$_{360}$-*b*-p(L)Cys(SO$_2$Et)$_{60}$ in DMSO-*d*$_6$.

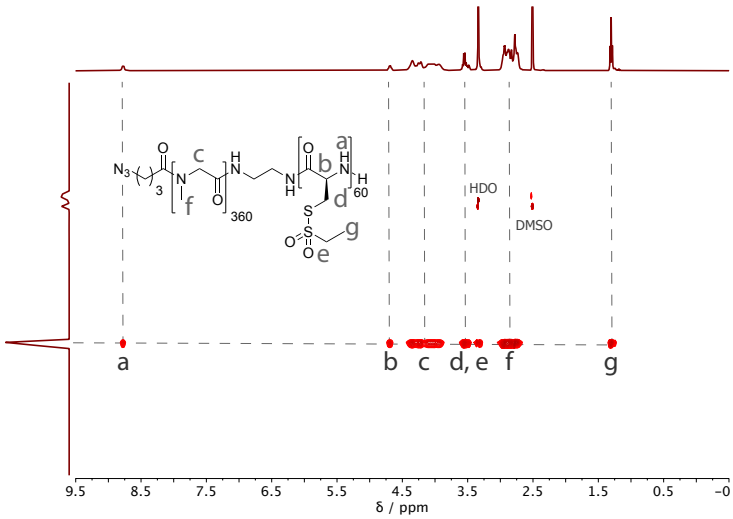

Figure S32. DOSY NMR Analysis of pSar$_{360}$-*b*-p(L)Cys(SO$_2$Et)$_{60}$ in DMSO-*d*